EES Batteries

Check for updates

Demonstration of and future perspective on scaling ultrafast-laser-ablation microstructuring of Li-ion battery electrodes to roll-to-roll production and large-format cells

Ryan J. Tancin,*[a] Bertan Özdoğru,[a] Nathaniel Sunderlin,[a] Peter J. Weddle,[a] Francois L. E. Usseglio-Viretta,[a] David R. Boone,[b] Quentin Mocaer,[c] Eric Audouard,[c] Kevin W. Knehr, [ID][d] Joseph J. Kubal,[d] Shabbir Ahmed, [ID][d] Donal P. Finegan [ID][a] and Bertrand J. Tremolet de Villers [ID][a]

This work demonstrates integration of an ultrafast laser onto a roll-to-roll machine, the laser structuring of a double-sided, 700 m long roll of graphite battery anode and its subsequent manufacture into 27 Ah prismatic cells. The electrode was ablated with a novel hybrid-microstructure composed of both hexagonally arranged pores for enhanced rate performance and channels for fast electrolyte wetting. Subsequently, this anode and a non-ablated baseline anode are paired with an NMC111 cathode for cell building and electrochemical characterization. Compared to the baseline, laser ablated cells demonstrated a reduction in soaking time of at least 60%, an improvement in fast charge capability with >30% more capacity accepted during 6C charging, and an extension of cycle life of >40% during 0.5C cycling. Further, a perspective is provided on scaling ultrafast laser ablation of battery electrodes to industrial throughputs. Additionally, lessons learned from this pilot-scale demonstration are provided in regards to optical architecture, debris removal, and system control. A techno-economic analysis is used to demonstrate that laser ablation can be integrated into existing electrode manufacturing facilities with only ≈$1.3 per kWh increase (≈2%) in manufacturing cost. Preemptive electrode design for laser ablation is discussed as a further method for enhancing performance. Finally, an analysis of available laser systems and beam-scanning architectures is used to determine design requirements to scale process throughput to a state-of-the-art speed of 50 m min^{-1}. This analysis demonstrates that laser ablating Li-ion battery electrodes has multiple benefits to manufacturing and battery performance, that the technology already exists to achieve high laser-ablation throughputs, and that integrating ultrafast laser ablation to electrode manufacturing will not create a cost or processing bottleneck.

Broader context

Li-ion batteries (LIBs) are critical to meeting future energy demands for consumer/personal electronic devices, transportation and stationary power storage and stabilization. LIB electrodes with engineered microstructures created by ultrafast laser ablation have been shown to provide the next step-change improvement in battery performance, including, charge rate, capacity, and cycle life. However, there remains a lack of R&D work which helps bridge the gap between the laboratory and factory. This work contributes towards this effort through demonstrating that an ultrafast laser can easily be integrated into industry standard electrode manufacturing equipment (roll-to-roll manufacturing). Both sides of a double-sided 700 m long graphite anode are laser patterned, and the electrode was subsequently assembled into 27 Ah cells (the largest to date incorporating a structured electrode). Lessons learned from this pilot demonstration are summarized and future recommendations are provided. We additionally provide a technoeconomic analysis which concludes that this additional manufacturing step results in a 2% increase to manufacturing costs. Finally, we analyzed various optical scanning architectures, and the direction of the industrial laser market, to provide recommendations on scaling this process to industry state-of-the-art processing speeds.

[a]*National Renewable Energy Laboratory (NREL), 15013 Denver West Parkway, Golden, CO 80401, USA. E-mail: ryan.tancin@nrel.gov, donal.finegan@nrel.gov, bertrand.tremolet@nrel.gov*

[b]*Clarios, Florist Tower, 5757 N Green Bay Ave, Glendale, WI 53209-4408, USA*

[c]*Amplitude, 11 Avenue de Canteranne, 33600 Pessac, France*

[d]*Chemical Sciences and Engineering Division, Argonne National Laboratory, 9700 S. Cass Avenue, Lemont, IL, 60439, USA*

1 Introduction

Historically, ultrafast lasers were complex, large, expensive and required specialized knowledge and meticulous care to operate and maintain, relegating them to narrow scientific or niche applications.[1–3] However, in the past decade there has been rapid development of ultrafast-laser technology, yielding substantial gains in time-averaged power, reliability, stability, and reductions in size and cost. These lasers are on the cusp of adoption for industrial use in mass producing intermediate goods. Notably, ultrashort light pulses can ablate material nearly athermally, making ultrafast lasers of interest for cutting or structuring thermally sensitive materials. Ultrafast laser ablation of Li-ion battery electrodes is one such application that has received considerable attention in the literature. The athermal ablation of electrode materials allows for cutting or creating 3-D electrode geometries, without inducing harmful changes to the local electrode morphology or the crystallographic structure of the active material, yielding higher-quality microstructures.

The laser ablation of engineered microstructures (either with ultrafast or long-pulsed lasers) has been demonstrated to great effect in the literature. Particularly of interest to this work are efforts where laser-ablation was used to enhance electrolyte wetting and/or high-rate performance and energy density in Li-ion battery electrodes. It has been well demonstrated that channel-like structures have a capillary effect, which aids in infiltration of the electrolyte in the electrode microstructure.[4–10] Thus, laser-structured electrodes require dramatically reduced times to achieve a similar or greater degree of wetting compared to their unstructured counterparts thereby reducing manufacturing time and cost.[5,10,11] Additionally, research suggests that laser-structured electrodes achieve more complete wetting compared to unstructured controls,[5,9,10] even when the latter is afforded a significantly longer wetting time.[8] This is particularly important for thick (i.e., ≥100 μm) or low porosity electrodes,[8] leading to better capacity utilization, cycle life, and rate capability.[9,10] Dry or partially wetted electrode areas often result in inhomogeneous current densities and overpotentials which can nucleate various degradation processes, such as lithium plating.[12] Hence, wetting-enhancing microstructures often lead to better cycle-life, particularly for cells cycled at higher C-rates.

While more thorough wetting can explain some beneficial effects realized in laser-ablated electrodes, it is likely that the engineered microstructure has additional benefits beyond improved wettability. The laser-ablated channels themselves also improve the through-electrode Li-ion transport by providing a less tortuous pathway between the seperator and active material. These electrolyte "highways" promote more homogeneous through-plane electrode utilization, resulting in lower degradation-promoting overpotentials.[13] More homogeneous electrode utilization is a primary reason why laser-structured electrodes exhibit longer cycle-life and improved reversible capacity when cycled at high C-rates compared to their unstructured counterparts. Further, laser-ablation enables the fabrication of thicker electrodes without the trade-off of reduced rate capability and prohibitively long wetting times, leading to cells with increased energy and power density.[14–16]

Laser ablation has emerged as a powerful technique for optimizing electrode architecture, enabling the fabrication of structured patterns that enhance electrochemical performance. Among these designs, different patterns have been suggested as "optimal". For example, a pattern of hexagonally arranged pores was determined by to be optimal[17,18] for maximizing rate performance with minimal material removal and has thus become a common choice for structured electrodes. This pattern has been used across numerous studies, demonstrating its ability to dramatically enhance cell rate performance[16,19] and enable thicker electrodes, leading to greater cell-level energy density.[7] Alternatively, mud-crack-like designs have been suggested to effectively improve electrode wetting dynamics, but have not been yet experimentally investigated.[18]

The benefits of ultrafast-laser ablated microstructures have been demonstrated across a wide range of Li-ion battery anode and cathode materials, including graphite,[11,13,20–24] $LiNi_xMn_yCo_zO_2$ (NMC),[10,20,25–27] $LiMn_2O_4$ (LMO),[28] $LiCoO_2$ (LCO),[29] $Li_4Ti_5O_{12}$ (LTO),[20] silicon,[20,30] and $LiFePO_4$ (LFP).[20,31,32] Despite the numerous advantages of laser-structured Li-ion battery electrodes, significant challenges remain in scaling up from laboratory demonstrations to full-scale industrial production.

One such challenge is achieving faster processing speeds. Achieving this will almost certainty involve adopting lasers with higher time-averaged powers. Work towards this end was demonstrated by Hille et al.[33] who used a picosecond laser (10 ps pulse duration) with a max time averaged power of 160 W in both continuous operation (≥1 MHz), and pulse-bust mode (82 MHz pulse frequency, 200 kHz burst frequency) to structure graphite anodes. Pfleging's group has published work using a high-repetition rate (up to 48.8 MHz) and high average-power (330 W) ultrafast laser (600 fs pulse duration) to structure various battery electrodes.[24,34,35]

New or adjacent technologies are also being explored to increase process throughput. Both Hille et al.[33] and Meyer et al.[24,36] have experimented with diffractive optical element (DOE) beam splitters to split a single laser beam into an array of beams, enabling parallel ablation of multiple features. The former involved Habedank et al.[37] published work on an improved control algorithm that provides enhanced temporal accuracy for coordinating a high-repetition rate laser with a fast beam scanning system. Such a system is necessary for maintaining acceptable pattern quality at high-throughput processing conditions. Jaeggi et al.[38] have similarly worked to head-off laser-scanner coordination challenges with a 50 W picosecond laser and a polygon scanner at surface speeds up to 100 m s^{-1}. To the best of our knowledge, a scanning speed of 20 m s^{-1} is that fastest example in the literature that has been applied to Li-ion battery electrodes which was achieved using a galvanometer (galvo) scanner.[35] The potential for faster speeds was demonstrated by Loeschner et al.[39] and

Schille *et al.*[40,41] who used polygon scanners to ablate non-battery materials with 100 W and 270 W ultrafast lasers at speeds of 800 m s^{-1} and 1000 m s^{-1}, respectively. It is important to note that the results depend greatly on the type of material, as the ablation efficiencies can vary from 0.2 to 12 mm^3 min^{-1} W^{-1} depending on the active material and/or the metallic substrate.

Laser-structured electrodes performance benefits are now being demonstrated in larger cell formats, relevant to applications demanding high-energy density such as in electric vehicles.[16,35,42,43] To the best of our knowledge, the previous largest cell constructed with laser-structured electrodes were a series of multi-layer pouch cells by Meyer *et al.*,[35] each with a capacity of $\approx$20.2 Ah.

Finally, recent research and emerging perspectives now position ultrafast-laser processing as a viable and integral technology for large-scale factory implementation. For example, there have recently been demonstrations of ultrafast-laser ablating electrodes on industrially relevant equipment, namely, roll-to-roll (R2R) machines.[35,44] Hille *et al.*[45] investigated the optimal location in the manufacturing process to integrate laser processing for maximum efficiency and effectiveness. Pilot-scale demonstrations are still needed to aid in bridging the gap between laboratory work and LIB factories.[46]

In the present work, we seek to further industrial adoption of laser-ablated Li-ion battery electrodes by completing a pilot-scale demonstration of roll-to-roll ultrafast-laser ablation. To the best of our knowledge, this work is the first to pass the following milestones *en route* to industrial adoption:

1. The largest area of microstructured electrode with an ultrafast laser in a single production run ($\approx$168 m^2).

2. The longest running single demonstration of ultrafast-laser structuring of a battery electrode ($\approx$3 weeks, with minimal stops for maintenance and quality control checks).

3. The highest capacity Li-ion battery built with a laser-microstructured electrode (>27 Ah).

4. The first prismatic Li-ion battery containing a laser-microstructured electrode.

Specifically, we demonstrate that a high-power ultrafast laser can be readily integrated with a standard R2R processing machine with minimal modifications. A 700 m long, double-sided, graphite anode was wound onto the R2R machine and laser ablated with a novel hybrid pattern which was dual-optimized for both fast wetting and high-rate performance. We discuss in detail many of the mishaps, mistakes, and lessons learned which may be useful for those replicating or building upon our work. Finally, the laser-structured graphite anode was paired with an NMC111 cathode and manufactured into $\geq$ 27 Ah prismatic cells for subsequent electrochemical testing. Control cells containing unstructured anodes were also constructed for comparison. Wetting times were compared between cells with laser-ablated anodes, the non-ablated control and the non-ablated control with 3 h additional soak time. Cells then underwent rate-sweep tests, and cycle life testing at both 4C and C/2. A techno-economic analysis is conducted to ascertain the economic impact on introducing

ultrafast laser ablation into the manufacturing process and preemptive electrode design is discussed as a way to further enhance cell performance.

We also provide a perspective on scaling this process to industrially relevant throughputs, specifically, 50 m min^{-1} for a 120 mm wide graphite anode. In this perspective, we determine the operating parameters for the emerging "kW class" of near-IR (NIR) ultrafast lasers, and select commercially available optics to obtain realistic values for parameters such as the (1) total transmission of the optical system, (2) expected focal spot size, and (3) scan-field size. Next, we analyze different beam-scanning systems including galvo-scanners, polygon scanners, resonant scanners, solid-state optical deflectors, and diffractive optical elements to assess their performance and suitability for high-throughput processing. This analysis indicates that there are no technological limitations to achieving electrode structuring at a throughput of 50 m min^{-1}.

2   Design considerations and experimental setup

In the course of this work, we identified 6 primary considerations for the design and integration of laser microstructuring into state-of-the-art battery manufacturing lines. These considerations are discussed in the following sub-sections.

2.1   Process integration

Ideally, ultrafast-laser microstructuring of Li-ion battery electrodes will be integrated into existing electrode manufacturing equipment, namely, the R2R machinery used for other processes (*e.g.*, coating, drying, calendering, *etc.*). Incorporating laser-ablation "in-line", is expected to minimize additional capital expenses and reduce the downtime associated with transferring electrode rolls between machines. Further, laser-ablation should not become a production bottleneck for other manufacturing processes, or force changes in processing conditions. An example of the latter would be forcing the electrode web to be processed with intermittent motion, which could interfere with other processes already optimized for continuous motion.

An important consideration is the location of the laser patterning step in the manufacturing R2R process. Hille *et al.* discusses this at length.[45] To summarize, laser patterning after coating (but before solvent drying) results in less energy needed to remove a given amount of material, but at the expense of poor pattern resolution and pore clogging, both of which severely reduced the efficacy of the ablated microstructures. Similarly, ablated microstructures formed after solvent drying but prior to calendering were somewhat deformed by the calender rolls, though, electrochemical performance appeared to be unaffected. Pore morphology was found to be unaffected if the laser-ablation step is integrated after electrode calendering, yielding the highest process precision.

2.2 Safety

Laser ablation must not effect surrounding factory work. Hence, laser ablation should occur inside of an interlocked, class-4 laser enclosure. Further, fine particulates are an inhalation risk to workers. The laser enclosure should also serve to contain any produced particulate matter.

2.3 Debris management

A substantial amount of debris is produced during laser ablation. For the work described here, approximately 900 g of graphite debris was produced during ablation. This material cannot be allowed to contaminate the electrode or build up inside of the laser enclosure. Air-jets and vacuum systems are typically (and successfully) employed in laboratory-scale laser scribers to remove debris and prevent electrode contamination.[5,20] These systems are readily scalable to industrial applications if properly designed and sized. Further, some form of material separation is recommended, such as cyclone separation, to remove ablated debris from the gas flow. It has been demonstrated that the debris produced during ultra-fast laser ablation of graphite electrodes can be directly reintroduced into the slurry making step, completely eliminating the cost associated with material loss.[21] Further, it is economically favorable to recover critical materials, such as the metals in NMC cathodes.

2.4 Laser system

Selecting the correct laser plays an outsized role in the efficiency, quality, and throughput in laser-ablating Li-ion battery electrodes. Regarding throughput, laser processing must keep pace with other manufacturing processes to prevent a bottleneck in the production line. This is especially true if laser processing is integrated onto the same R2R machine as these other processes. With state-of-the art electrode coating speeds now reaching peak speeds of 100 m min^{-1},[47–49] ultra-fast-lasers with high time-averaged powers are required to achieve the specified material removal rate.

Choosing the optimal laser wavelength is also critical to successful in-line laser-ablation technology. First, the electrode materials' absorption of laser-light varies with wavelength, with higher absorption coefficients at the laser's wavelength generally leading to better ablation.[50,51] However, selecting a particular laser wavelength must be balanced with market availability. For example, more efficient ablation for a material may occur near 515 nm, but lasers at this wavelength typically utilize frequency doubling of the 1030 nm fundamental wavelength, resulting in a power loss on the order of a factor of two. Hence, higher throughout might be achieved by using the higher power fundamental frequency despite its lower ablative efficiency.

Choosing common laser types such as Yb-YAG and Nd-YAG (fundamental frequencies near 1030 nm and 1064 nm, respectively) offers many advantages including (but not limited to) having a large number of competitively priced lasers with high-powers and a variety of specifications to choose from as well as a wide array of commercially available optics optimized for these wavelengths.

Laser wavelengths in the near infrared or shorter are recommended because these can be focused to a spot size near the target size of laser-ablated features (i.e., 10–50 μm). Longer wavelengths require shorter focusing lenses to maintain an adequate laser spot-size, which limits the field-of-view of the laser scanning system and reduces the depth of focus. Shorter wavelengths can maintain a small spot-size using a long focal-length lens. However, a smaller-spot size is typically achieved at the expense of power loss during frequency conversion.

2.5 Beam scanning and optical architecture

The beam scanning architecture plays a crucial role in ensuring high-quality ablated microstructures while simultaneously sustaining the required processing speed. At state-of-the art processing speeds (e.g., 50 m min^{-1}), beam scanners must be able to ablate 10s of millions of features per minute, and do so with high-spatial and temporal accuracy. The optical design must ensure a sufficiently focused laser to precisely ablate features of the desired spot-size. This is discussed in detail in section 6.

A related consideration is ensuring that the electrode web is coplanar with the focal plane of the focusing lens to achieve consistent microstructure morphology across the electrode. Ideally, this is done by adjusting the electrode web position to eliminate to need to realign optics when compensating for different electrode thickness.

2.6 Quality and operational control

Periodic assessment of the laser-ablated microstructure is necessary to ensure pattern quality and to rapidly identify problems with the laser or optical systems. Pattern quality control can be completed after an electrode roll has been ablated through microscopy or optical profilometry in the factory's metrology lab. Real-time monitoring is necessary to (1) prevent misaligned patterns resulting from drift in the electrode web position, (2) compensate for electrode web speed fluctuations, and (3) to shut off the laser system in the event that the R2R machine stops due to a fault during processing.

3 Experimental methods

3.1 Electrodes

A graphite anode and LiNi$_{0.33}$Mn$_{0.33}$Co$_{0.33}$O$_2$ (NMC111) cathode were used to construct cells in this work. The graphite anodes included two, double-sided, 700 m rolls, one of which was laser-structured and the other was used as a baseline. Each electrode consisted of 96% graphite, 3% styrene butadiene rubber (SBR) and carboxymethyl cellulose (CMC) binder mix (1 : 1 ratio), and 1% conductive carbon, by mass. The anode slurry was coated onto a 12 μm thick, 130.65 mm wide copper foil current-collector at a width of 118 mm. After drying and calendering, the electrode coating had single-sided thickness, loading, and porosity of 75 μm, 3.15 mAh cm^{-2}, and

37%, respectively. The electrode selected for laser ablation had ≈6% of its coating mass removed during the process, resulting in a new loading of ≈2.99 mAh cm^{-2}. Fig. 1a illustrates the hybrid laser-ablated microstructural pattern ablated into the anode (discussed further in section 3.4).

The NMC cathode was also double-sided, and consisted of 95% NMC111, 2% polyvinylidene difluoride (PVDF), and 3% conductive carbon. Cathodes were slurry coated onto a 131.7 mm wide, 15 μm thick aluminum current collector at a coating width of 112 mm. Post-fabrication, the single-sided coating was 67 μm m thick with a loading of 2.64 mAh cm^{-2} and porosity of 32%. In this study, the cathodes were not ablated.

Prismatic cells with nominal minimum capacity of 27 Ah were manufactured by Clarios at their pilot facility (see Fig. 1b). The N/P ratios of 1.19 and 1.13 were achieved for baseline and laser-ablated cells, respectively.

3.2 Roll-to-roll setup

Anode laser micro-structuring was demonstrated on NREL's metrology R2R machine (Killion WS-18G, Davis standard, LLC). An enclosure constructed of matte-black anodized aluminum sheets was constructed around a portion of the R2R machine to prevent laser-radiation exposure (pictured in Fig. 2a and b). The aluminum was ≈3 mm thick, which was designed to withstand direct exposure of the unfocused laser beam at full power. Most surfaces inside the enclosure had a matte surface to minimize the potential for specular reflections of laser light during beam alignment. All doors on the enclosure were interlocked to the laser to prevent accidental laser exposure. A pair of E-stop buttons enabled easy laser-shutoff in the event of an emergency and a lab-wide emergency power-off button was installed to stop both the laser and the R2R machine in the event of an emergency. The laser interlock for the main enclosure door was disconnected during beam alignment and was wired to the interlock on a mobile enclo-
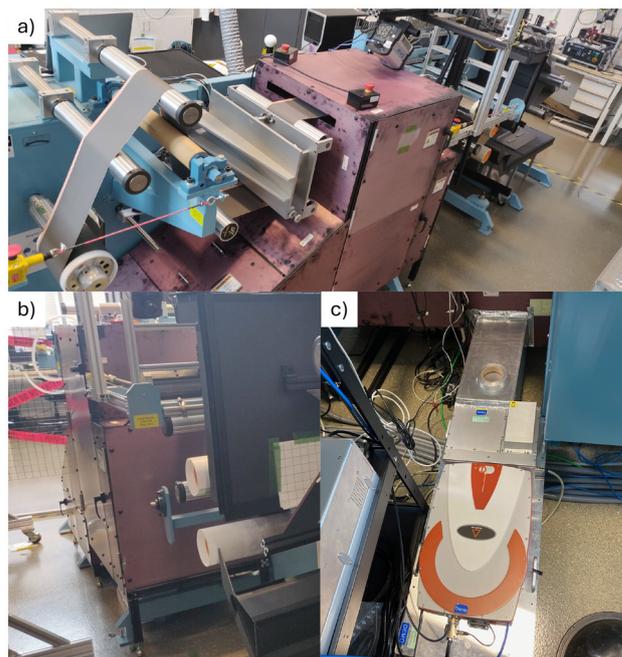

Fig. 2 (a and b) NREL's metrology R2R system with a light-tight laser enclosure integrated onto the system. (c) The ultrafast laser integrated into the laser enclosure.

sure constructed from laser-safety curtains, which allowed space for up to two workers to align the optical system and observe test ablation. Space constraints required that the laser to be bolted to a small platform and connected to the enclosure *via* a light-tight tunnel, pictured in Fig. 2c. The electrode web and electrical connections were fed into and out of the enclosure through a series of baffles to create a torturous path preventing light reflections from escaping. The right side of Fig. 3a shows an example of the light baffle section designed to reduce light reflections.
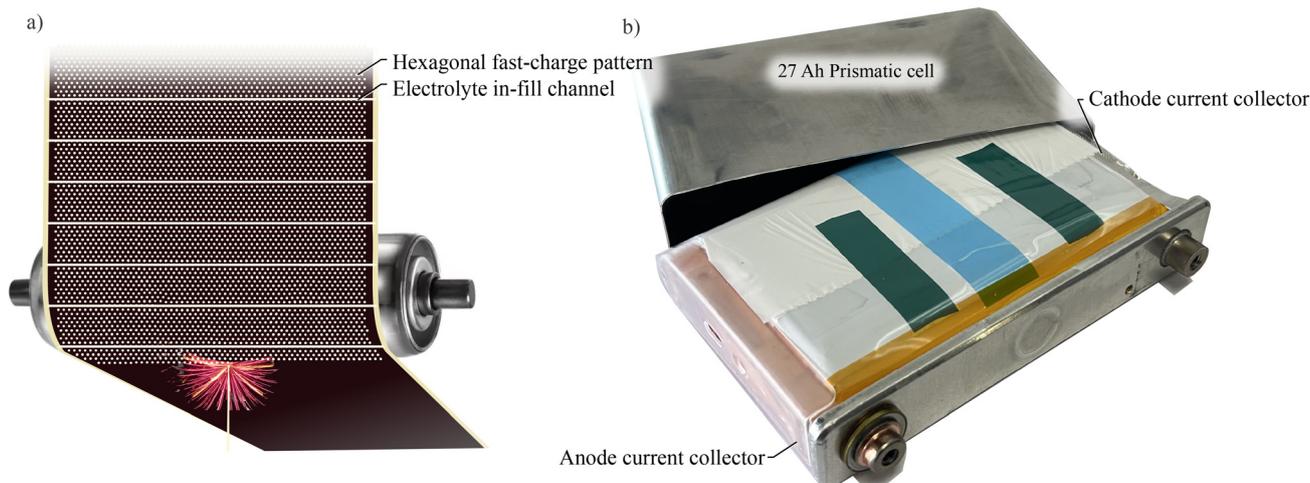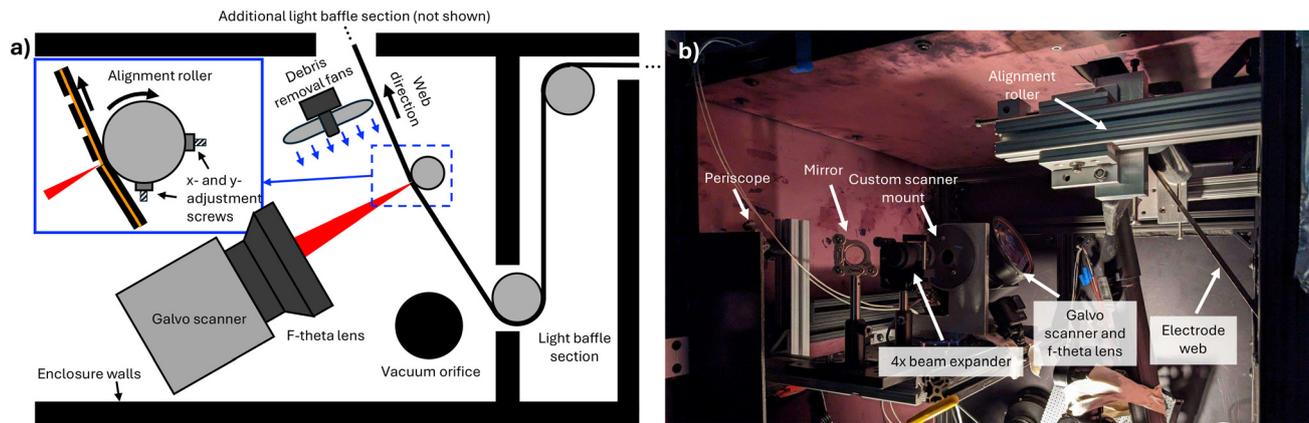

Fig. 1 (a) Intended laser-ablation design on the graphite anode electrode. (b) 27 Ah prismatic cell manufactured at Clarios's pilot facility.

© 2025 The Author(s). Published by the Royal Society of Chemistry

Fig. 3 (a) Schematic detailing the position of the electrode web in relation to the optical setup, debris removal hardware, and alignment roller. (b) The optical setup inside of the laser enclosure.

3.3 Laser and optical setup

The laser used presented in the present manuscript was a diode-pumped, fiber-based, ytterbium-doped yttrium-aluminum-garnet (Yb:YAG) laser (Amplitude Satsuma HP^2). The laser had a center wavelength of ≈1030 nm, a pulse duration of ≈277 fs, and was operated at a repetition rate (f_{rep}) and pulse energy of 333 kHz and 60.7 μJ, respectively. The resulting time-averaged power at the laser aperture was 20.2 W. The power loss between the laser aperture and electrode web due to transmission and reflectivity losses was measured to be <10%.

Fig. 3a shows a schematic of the optical setup inside the laser enclosure. Noticeably, the electrode web passed through the enclosure at an approximately 60° angle from horizontal. This was not ideal for alignment of the optical system but was necessary because the enclosure was reused from a prior project with different geometric requirements. The laser beam was directed to a small optical breadboard (pictured in Fig. 3) near the electrode web using dielectric ultrafast mirrors with a 1030 nm design wavelength (Edmund Optics, 85-102). Arriving at the optical breadboard, the laser beam had a $1/e^2$ diameter of ≈ 2.5 mm. A 4× telescopic beam expander (Edmund Optics, Vega 19-404) increased the beam diameter to 10 mm to enable the beam to be focused to a smaller spot-size. The laser beam was immediately passed into a dual-axis, galvo, laser-scanning head (ThorLabs, XG220-Y1) with near-infrared optimized mirrors. Subsequently, the laser beam was focused by a fused-silica, f-theta lens (VONJAN Technology, F-206H-1030-1080) with a focal length of 206 mm and a maximum scanning area of 120 × 120 mm. The final focused laser spot size was ≈ 31 μm.

To achieve uniform ablation efficiency and microstructure resolution, it was critical that the electrode be kept co-planar with the f-theta lens' focal plane during processing. This was achieved by adding an additional "alignment roller" to the R2R machine, which slightly pushed the electrode web towards the f-theta lens (illustrated and pictured in Fig. 3a and

b, respectively). The X and Y positions of each end of the roller's axle were adjusted using a pair of adjustment screws resulting in 4 degrees of freedom. The roller was aligned by ablating a row of pore features across the width of a spare electrode web and subsequently examining the pattern under a microscope. The roller was first made parallel with the lens' focal plane by observing if the ablated pore diameter was consistent across the electrode web. Misalignment of the roller resulted in small pores closest to the laser focus and larger pores further from the focal plane. Adjustments were made until the feature size was consistent across the electrode. Finally, the roller was translated perpendicular to the lens' focal plane until the diameter of ablated pores was minimized.

3.4 Hybrid microstructure

The graphite anode was ablated with a hybrid microstructure consisting of both channels to enhance electrolyte wetting speed and quality and hexagonally arranged pores to enhance charge-rate capability for minimum material removal. Fig. 6a and b shows optical microscopy and optical sectioning topography images of the hybrid microstructure, respectively. Specifically, the pattern consisted of a 10 row repeating pattern, with 9 rows of hexagonally arranged pores followed by a single continuous channel. The spacing between rows was 125 μm and the pore-to-pore spacing within a row was 240 μm, yielding an irregular hexagon pattern.

The optimal pore network (for fast charging) and channel network (for fast wetting) geometries have been identified in previous modeling work[18] using a genetic algorithm. For pores, the optimal geometry is the one used in the manufacturing process: holes organized along a regular hexagonal pattern. This architecture minimizes the average distance from any point within the porous electrode matrix to the channels, as the benefit from these channels is only effective for regions of the electrode near a channel. For the channel network, the optimal geometry predicted by the model in[18] is a mud-crack-like pattern. The latter cannot be reproduced easily in a manu-

facturing line, therefore the simpler 1D lines have been used instead. However, the two configurations (mud-crack-like pattern and 1D lines) have been compared in previous work[18] and the 1D lines architecture is near optimal.

Similarly, the selection of the channel spacing is derived from previous modeling work.[18] Results indicated that channels required much less material removal to achieve a given level of benefit to electrolyte wetting compared to pore features with the same amount of mass removal. This indicates that, for pores and channels with similar diameters and widths, a combined pore and channel pattern would consist in relatively few channels spaced far apart from each other, with relatively more pores located in between channels. That is essentially a superposition of the two patterns. We have also performed electrochemical macroscale simulation in COMSOL to tune the channel spacing (unpublished).

The pore depth was targeted as half the thickness of the single-sided electrode coating because it has been demonstrated in the literature that there is minimal further benefit to performance for the increased material loss from laser ablation.[52,53] Further, deeper features will increase the manufacturing time needed to create these microstructures. The channel width and pore diameter was a result of (1) using a long focal-length scanning lens so that a single scanner could be used for the entire width of the electrode, (2) the maximum laser beam size which could be accommodated by the galvo-scanner and scan lens, and (3) the ablation characteristics of the graphite electrode coating in which particle size has been shown to effect feature dimensions.[20] Finally, the row-to-row spacing and pore-to-pore spacing was chosen for practical reasons including processing time (the R2R machine was shared with other research projects), the buffer size of the function generator controlling the laser and the minimum web speed.

3.5 Operation and control

The R2R machine was run at a speeds of either 0.061 or 0.091 m min^{-1}. The first side of the electrode was processed at a speed of 0.091 m min^{-1}. However, due to optic fouling and lower than expected ablation depths the speed was reduced to 0.061 m min^{-1} for the opposite side of the electrode (discussed further in section 4.1). These speeds represented the lower limit of the R2R system's operational capability. Running at a minimum web speed meant that velocity and tension control was relatively poor, resulting in fluctuations in the pattern period of ≈±50%.

Throughputs of 0.061 and 0.091 m min^{-1} corresponded to 8 and 12 scans per s, respectively. The focused laser spot was scanned across the width of the electrode web (x-direction) by the dual-axis galvo in alternating directions to ablate each row of the hybrid microstructure. Each axis of the galvo scanner was controlled by a separate channel of an arbitrary function generator. A triangle wave commanded the x-axis to scan across the electrode, while a sawtooth wave commanded the y-axis to compensate for the web motion during a scan and subsequently advance the laser spot to the next row.

Discontinuous velocity or acceleration commands to the galvo scanner resulted in large current draw from the servo motors, which could lead to excessive heat buildup (and premature wear) as well as poor pattern quality due to setpoint overshoot. Hence, each waveform sent to the galvo scanner was smoothed to provide a continuous, finite acceleration profile.

A second function generator commanded the acousto-optic modulator (AOM) inside the laser head, which was used to gate the laser output. The output was blocked at the end of each pattern row so that no ablation occurred during mirror acceleration. The patterned was extended ≈2 mm past the electrode coating edges to ensure that the electrode was completely patterned, while accommodating for some x-direction drift of the electrode during processing. Pores were ablated by turning the laser on and off with the AOM as it was scanned across the electrode with a 40% laser-emission duty cycle. The oblong pores this method produces can be made circular by controlling the x-axis to dwell at each pore location. However, controlling the x-axis dwell-time results in a severe and unacceptable processing speed reduction. The resulting average pore depth was 40–50 μm at 0.061 m min^{-1} and 30–40 at 0.091 m min^{-1}, respectively. The resulting mass removal for either side was 6.8% and 5.2%. Unfortunately, the arbitrary-function buffer size of the function generator controlling the AOM limited the number of pores that could be ablated per row. Hence, the microstructure was limited to a relatively coarse pattern with larger than optimal pore-to-pore spacing.[18]

3.6 Electrolyte filling and electrochemical impedance spectroscopy (EIS)

Dry cells were first evacuated, then filled with a proprietary carbonate-based electrolyte followed by a pressurized nitrogen gas pulse. In a dry room, EIS scans were collected using a Biologic SP-300 potentiostat to monitor time-dependent changes in cell impedance due to electrolyte infiltration. The cells were measured at open-circuit voltage in potentiostatic mode with applied alternating excitation voltage of 5 mV in two-step frequency sweeps: from 500 to 1 Hz with 18 frequencies per decade, then from 1 Hz to 50 mHz with 6 frequencies per decade. The experimental data were fit using the Python package "impedance.py" to extract time-dependent parameters such as the ionic resistance of the porous electrodes.[54]

3.7 Electrochemical cycling conditions

The cells were formed by applying 1.4 A (C/20) up to 2.6 V, followed by 2.7 A (C/10) up to 3.4 V, then 9 A (C/3) up to 4 V followed by constant voltage at 4 V until the current reduced to 0.5 A. The low voltage cutoff during formation was used to prevent excessive gassing and produce an ideal SEI layer. Each cell was then discharged at 9 A to 2.7 V followed immediately by charging again at 9 A to 3.55 V and held at constant voltage until the current reduced to 0.5 A. The formation capacity was measured during the 9 A constant-current discharge step. The cells were then rested for over 1 week before cycling began.

Cycling was conducted under various conditions to evaluate the cells' responses: (1) rate tests consisting of increasing

C-rates, (2) low-rate cycle life tests conducted at 0.5C, (3) moderate rate cycle-life tests conducted at 1C and 2C cycling, and (4) elevated rate cycling tests conducted at 4C. Cells were cycled between 2.7 V and 4.1 V. The relatively low operating voltage of 4.1 V for these cells was used to delay degradation at the cathode.

4 Results

4.1 Roll-to-roll pilot demonstration

Fig. 4a and b illustrates the graphite loaded on the R2R machine for laser processing and the electrode web being ablated, respectively. Laser processing began on the first side of the electrode at a speed of 0.061 m min^{-1}. Slight electrode web misalignments on each roller resulted in small (<5 mm) lateral drifts of the electrode web on the alignment roller. After ≈40 m, these misalignments were run out of the system and the web position stabilized. The misalignment could have been minimized by positioning the laser ablation directly after a web displacement guide, but this was not possible using the current machine design. The laser-ablated pattern was kept centered on the web by visually inspecting the pattern registration as the web exited the laser enclosure, and providing a DC bias to the galvo-control waveforms to re-center the pattern. The lag between observation and adjustment presents the possibility that the wetting channels did not fully extend to the edge of the electrode, blocking their access to the electro-

Fig. 4 (a) The 700 m graphite electrode wound on the R2R machine during processing. (b) Ultra-fast laser-ablation of a graphite test electrode on the R2R machine.

lyte and rendering them less effective. Hence, cells manufactured from the first 40 m of electrode were discarded.

Debris handling proved to be a persistent challenge during processing. The case fans and HEPA-filtered vacuum prevented any debris from contaminating the electrode. However, these systems did a poor job of removing debris from the enclosure. After processing about 80 m of electrode, debris collecting on the surface of the f-theta lens and other optics began to attenuate the laser light to the extent that the pattern was no longer visible on the electrode. Fig. 5 illustrates the fouled optics and enclosure. After 80 m, processing was stopped and the optics were cleaned. Initially, a tube was installed through the light baffles and connected to a nozzle to allow the R2R operator to clean the surface of the f-theta lens with a blast of compressed air without opening the laser enclosure and halting processing. When the electrode was flipped to process the opposite side, four positionable nozzles were installed to clean the f-theta lens, beam expander, and the two mirrors closest to the electrode web. Each was connected to a compressed-air manifold supplied by a timed solenoid, which provided a 5 s air-blast at 5 min intervals. After installing the compressed air manifold, optics fouling was no longer an issue. No debris was found on the electrode surface after processing.

Several other faults occurred during the pilot demonstration. One such fault occurred when the laser shut down for unknown reasons (potentially a power bump in the lab). Another fault occured because the electrode web tore at a location where there was severe current collector wrinkling and rough edges existed due to prior manufacturing steps. In these cases, the R2R machine was reversed to the location where the fault occurred, the web was re-spliced (if necessary) and processing was resumed with a small un-patterned gap left where the fault occurred. The pattern was not overlapped to avoid potentially damaging the current collector through over-ablation, compromising the web's strength. These locations were flagged so that cells made with these regions could be discarded.

Locations where the web had been previously spliced together had the potential to tear during laser ablation. Each splice was held together with tape on either side. The tape was effectively cut as the laser ablated the channel features onto the electrode. If the splice was not subsequently re-taped, the web would break during ablation of the reverse side. Splices were flagged so that cells made with these electrodes could be discarded.

4.2 Realized laser-ablated microstructure

Fig. 6a and b shows optical images and topographic maps of the laser-ablated electrode, respectively. Fig. 7 shows scanning-electron microscope micrographs of the ablated electrode sheets. The microstructure shown in these images is close to the intended microstructure in pattern dimensions. However, the pores had a noticeable oblong shape resulting from the 40% duty cycle needed to achieve the desired ablation depth. Fig. 7e and f shows detailed views of the non-ablated top of the electrode and the bottom of a laser-ablated channel,
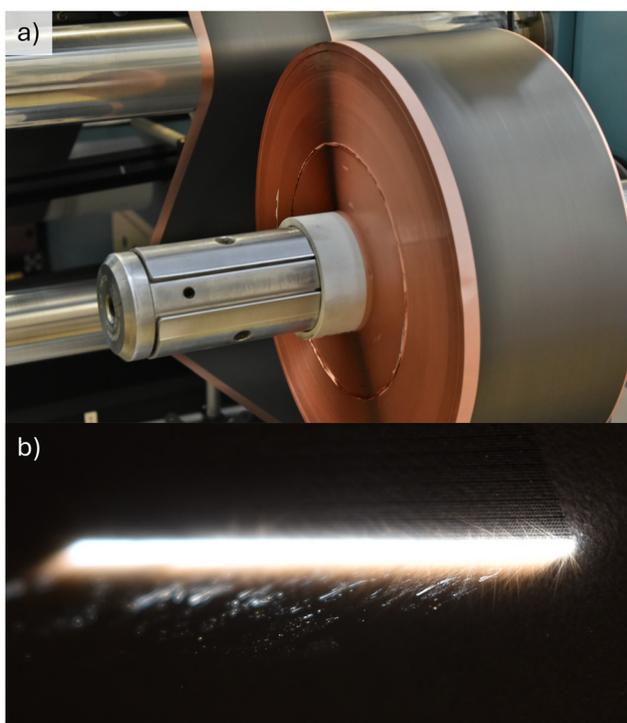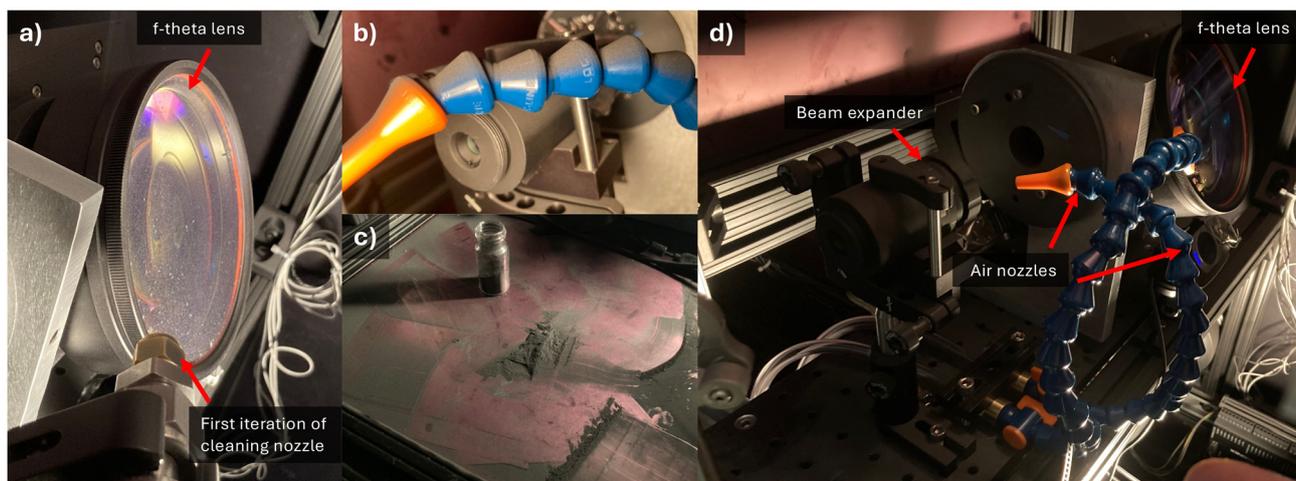
Fig. 5 Debris produced during laser ablation fouls optics and covers surfaces inside the laser enclosure. (a) The first iteration of the cleaning nozzle is aimed at the fouled f-theta lens. (b) Debris settled on the top of a cleaning nozzle and the beam expander. (c) Graphite debris is collected off the floor of the laser enclosure. (d) The enclosure is cleaned and position-able cleaning nozzles are installed between laser-processing runs.
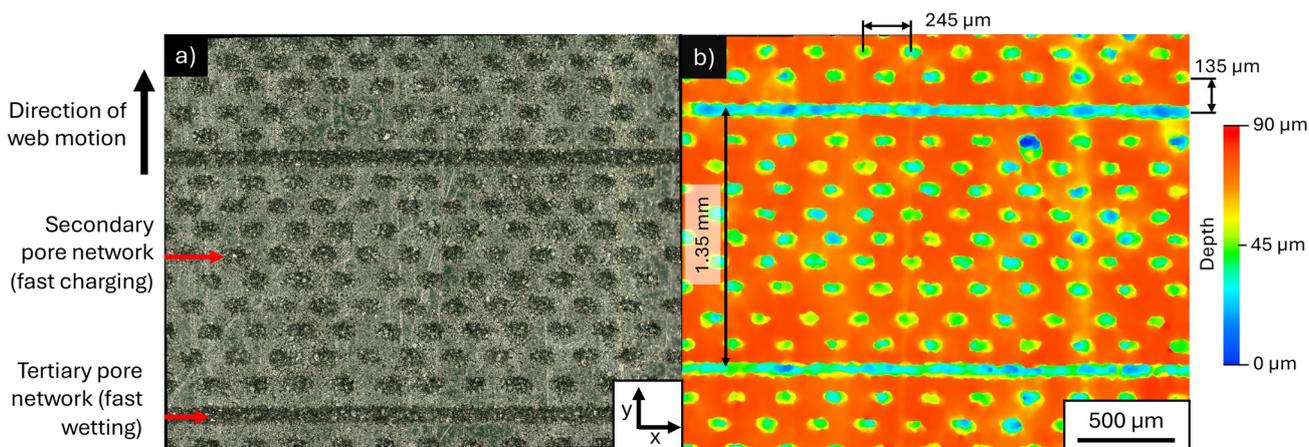
Fig. 6 (a) Optical and (b) optical sectioning topography images of the hybrid microstructure ablated onto the graphite anode.

respectively. As illustrated, no morphological changes or signs of thermal damage were observed in the graphite between these two regions despite exposure to high-power and high-repetition rate laser radiation. However, less binder and less conductive additive were observed at the bottom of the channel compared to the non-ablated electrode sections, and what additives were present appeared to be thermally effected. These results suggest that unlike graphite, the additional composite electrode materials are effected by the laser.

In contrast to the ideal microstructures shown in Fig. 6 and 7, most of the ablated pattern showed pronounced variation in the pattern period, resulting from by velocity fluctuations in the web speed. The web-speed velocity fluctuations were likely a result of poor tension control, particularly when running near the minimum web speed. Fig. 8 highlights pattern inconsistency between two sections of the electrode sheet. The inconsistent web-speed control could occasionally become so

extreme that two rows of pores overlap and form a channel-like feature.

4.3 Electrolyte wetting

Electrochemical impedance (EIS) was measured at several time points within the first couple of hours after electrolyte filling of the prismatic cells. Fig. 9a and b show Nyquist plots of the EIS data for the laser-ablated and non-ablated cells, respectively. Each dataset was fit (dashed lines) to a circuit model: $Z_{tot} = Z_b + Z_s + Z_{cr} + Z_p$, where Z_b is the impedance of the bus bars and current collector foils, Z_s is the separator resistance, Z_{cr} is the contact impedance of the interfaces, and Z_p is the porous electrode impedance. Because the imaginary component of the impedance, $-\mathrm{Im}Z < 0$ in some parts and has a non-infinite slope, Z_b was chosen to be a non-ideal inductor; Z_s is a resistor; Z_{cr} was chosen to be an RQ element in parallel where Q is a non-ideal capacitor or constant phase element; and Z_p was
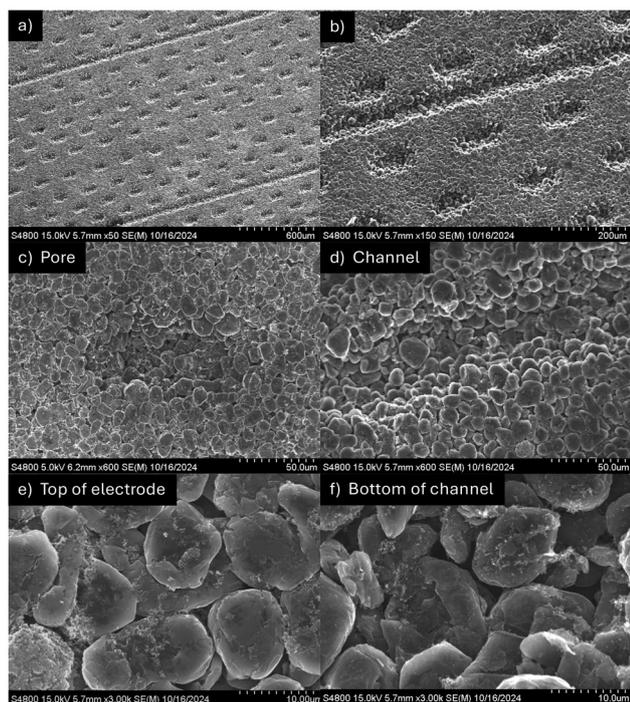
Fig. 7 (a,b) SEM micrographs of the laser ablated pattern from "side 1" including a detail of (c) a pore and (d) and channel. Details of the unablated top of the electrode (e) and the bottom of a laser-ablated channel (f) indicate that the remaining material was not damaged by the laser.
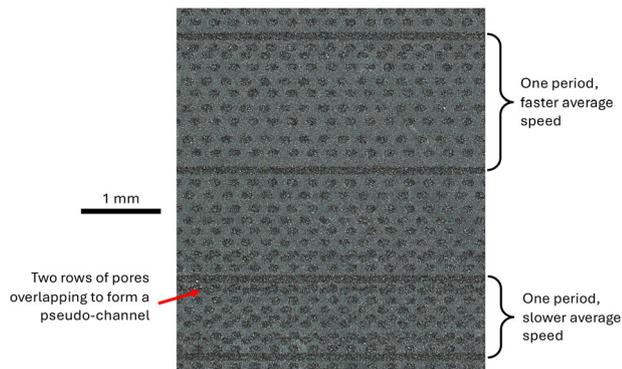
Fig. 8 Microscope image of a patterned electrode area severely effected by web-speed fluctuations.

chosen to be a transmission line model based on eqn (11) from the work of Landesfeind *et al.*[55]

Fig. 9c is a plot of R_s and R_p *versus* time after electrolyte fill. R_s is the value of the of the x-intercept from the Nyquist plots, and it is observed that for each cell, R_s decreases over time, indicating a lowering of the separator resistance as the electrolyte fills into the cell. The R_s of the laser ablated cell decreases from 6.18 to 5.58 mΩ and is always lower than the R_s of the non-ablated cell that decreases from 6.99 to 5.72 mΩ.

Similarly, R_p decreases as electrolyte infiltrates the porous electrode composites. In this case, R_p of the laser-ablated cell

is already near its minimum value, approximately 1 mΩ, by the time of the first EIS measurement at 10 min after fill, indicating that the laser-ablated microstructures enable rapid wetting. For the non-ablated cell, the initial R_p is much higher at 8.12 mΩ, and the data show a significant decrease to 1.09 mΩ takes approximately 40 min after fill, confirming a much longer wetting time is required in the non-ablated cell.

### 4.4 Formation, electrochemistry, and acoustic diagnostics

The formation cycle capacity measured during the C/3 discharge step (see Fig. 10a and b) shows that the laser-ablated cell capacity was consistently higher than the non-ablated cell capacity. As illustrated, the non-ablated cells showed a bimodal distribution in formation capacity, where one batch was given a 2 h rest time between filling and formation and the other around 5 h. The laser-ablated cells were each given 2 h between filling and formation. The laser-ablated cells with a 2 h rest time showed around 1.6 Ah more capacity than their 2 h non-ablated counter parts and around 0.3 Ah more capacity than their 5 h non-ablated counterparts. In addition to an increase in average capacity, the laser ablated cells showed less variation in capacity compared to the non-ablated cells. Fig. 10c illustrates differential capacity curves during the formation. There are several differences between the laser-ablated and non-ablated cells' dQ/dV responses, which are highlighted in magnified views in Fig. 10d. Region of interest 1 (see Fig. 10d) shows that the stage 2 (LiC$_{12}$) graphite peak is accessed at a lower voltage in laser-ablated cells, thus demonstrating a lower overpotential. The reduced N/P ratio in the cells with laser ablated anodes (*i.e.*, there is less anode active material in the laser-ablated cells compared to the unstructured anodes, while the same cathode is used for both) may also contribute to this shift. Region of interest 2 (see Fig. 10d) shows a considerably more prominent peak at 3.8 V during charge and an equivalent difference at the same voltage during discharge as shown by region of interest 3. This difference is attributed to greater access to the NMC cathode capacity, where wetting of the cathode may have slightly improved and thus allowed access to more cathode capacity in that voltage range. Region of interest 4 shows the shift in voltage where the stage 2 anode lithiation state transitions to graphite at a lower voltage (thus higher overpotential) for the non-ablated cells than the ablated cells.

In summary, the formation data shows that the laser ablated cells facilitate significantly faster wetting thus allowing reduced rest time between filling and formation, higher capacity which is attributed to superior wetting and thus less loss of active material, and reduced overpotential during charge and discharge.

4.5 Cycling

The cells were evaluated for their cycle life when exposed to charge rates of 0.5C and 4C, as well as a rate test sequence to evaluate their accessible capacity during the constant-current steps at rates up to 6C. The rate test, shown in Fig. 11a, includes a step increase in charge rate starting with 0.5C, fol-
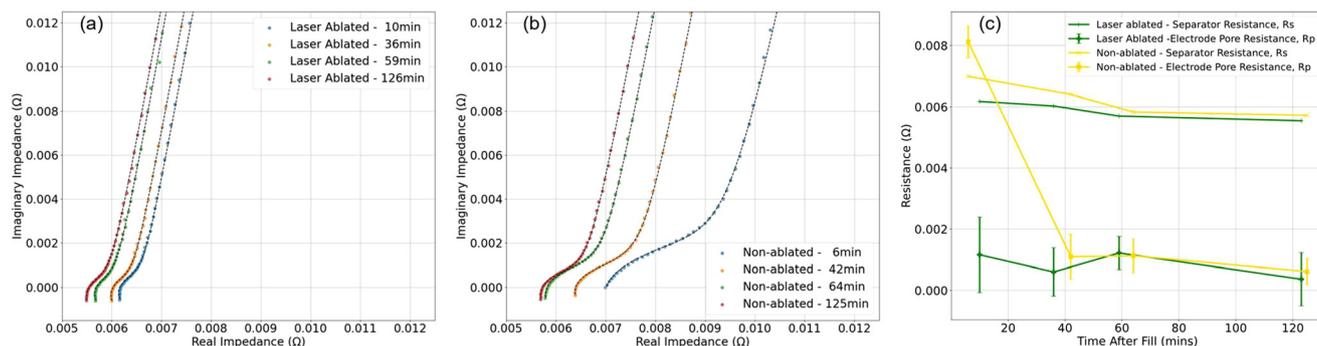
Fig. 9 Nyquist plots of impedance at 4 time points within the first 2 h after electrolyte filling for (a) laser-ablated and (b) non-ablated cells. (c) Separator resistance, R_s, and electrode pore resistance, R_p, as a function of time after electrolyte fill.
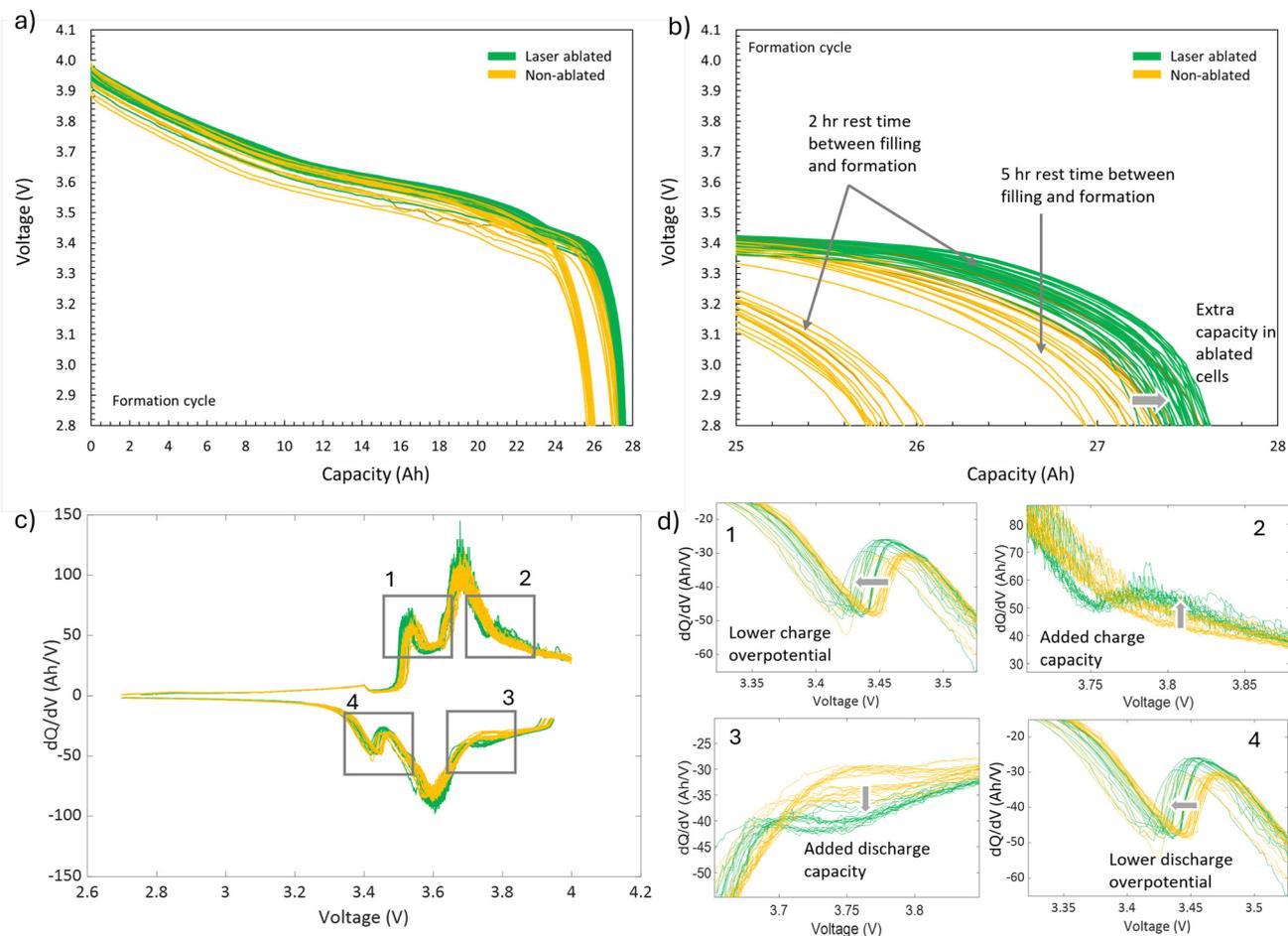

Fig. 10 Electrochemical data during formation showing (a) the discharge voltage *vs.* capacity plot with (b) magnified view of the of the low voltage region at the end of discharge, and (c) the dQ/dV plots during the first full cycle with (d) magnified regions of interest.

lowed by 1C, 2C, 4C, and 6C charging. After the 6C charge, the rate is returned to 1C and 0.5C to evaluate the cells' reversible capacity. All rates were evaluated over 5 sequential cycles before proceeding to the next rate. At 0.5C, no significant difference was observed in the achieved capacity with both cell types achieving 100% capacity of 28 Ah. At 2C and above, the

two cell types begin to diverge with the laser-ablated cells showing superior capacity. At 4C, the non-ablated cells achieve lower capacity and their capacity fades over the 5 cycles from 22 Ah to 20.5 Ah. At 6C, the non-ablated cells' capacity faded quickly from 16 Ah down to 11 Ah after just 5 cycles, whereas the laser-ablated cells maintained a slower fade from around
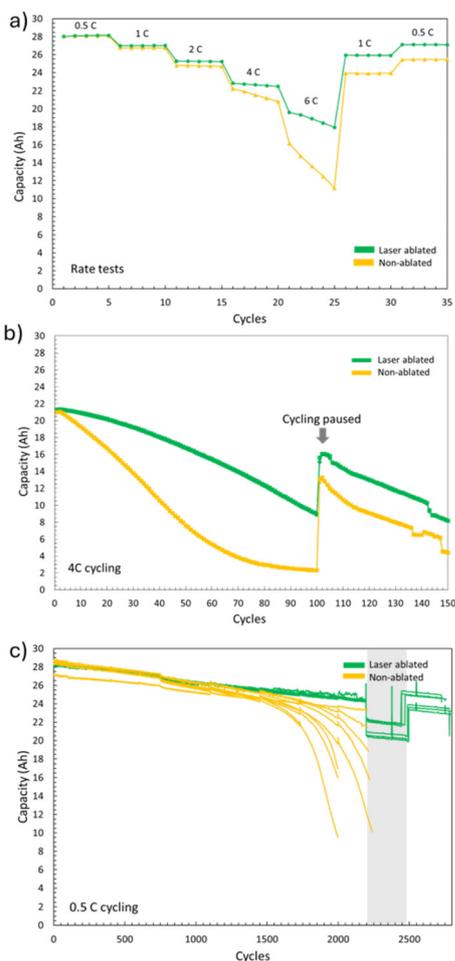
Fig. 11 (a) Capacity accepted during a series of increasing constant current charge steps to 4.1 V. (b) Cycle life capacity fade data during cycling with 4C constant current charge steps to 4.1 V and 0.5C discharge to 2.7 V. Cycling was paused to allow for relaxation at cycle 100 and then resumed. (c) Cycle-life capacity fade data during 0.5C cycling between 2.7 V and 4.1 V showing the drop-off in capacity for non-ablated cells after around 2000 cycles. The gray section represents a period where the cells were moved to a different facility and mistakenly operated at 1C charge rather than 0.5C.

19.5 Ah down to 18 Ah. By the 5th 6C cycle, the laser-ablated cells maintained 63% higher capacity compared to the non-ablated cells (*i.e.*, 18 Ah compared to 11 Ah). The rapid capacity fade indicates that Li plating occurred at 4C in non-ablated cells and equivalently in the laser-ablated cells at 6C (*i.e.*, the rate of capacity loss of non-ablated cells at 4C was equivalent to the ablated cells at 6C). Following the 6C step, the cells were returned to 1C and 0.5C, where the laser-ablated cells showed a capacity loss of around 1 Ah, while the non-ablated cells lost almost 3 Ah. This rate-capability test demonstrates that laser-ablated cells can achieve considerably more fast-charge capacity, while simultaneously being more resilient to Li-plating.

Fig. 11b shows the cycle-life evaluation for cells cycled continuously at 4C. The rate of capacity fade was significantly

higher for non-ablated cells. After 100 cycles at 4C, the capacity of laser-ablated cells decreased to 9 Ah compared to 2 Ah for the non-ablated cells. After rest (see jump in Fig. 11d at 100 cycles), the cell capacities recovered to 16 Ah for the laser-ablated cells and 13 Ah for non-ablated cells, indicating that both cell types underwent severe Li plating. However, the laser-ablated cells are able to retain more reversible capacity even at this abusive cycling condition.

The cycle-life capacity at a low rate of 0.5C was also evaluated (see Fig. 11c). The non-ablated cells started to diverge from the laser-ablated cells after around 1000 cycles, where their capacity fade began to accelerate and all but 1 non-ablated cell had reached it's "knee" by 2200 cycles. Conversely, none of the laser ablated cells showed any indication of accelerating capacity fade by 2800 cycles. Due to other project demands, all cells had to be removed from cycling and the exact cycle-number at which the "knee" occurs for the laser-ablated cells could not be determined. The extended life of the laser-ablated cells is attributed to the laser ablated features acting as local reservoirs of excess electrolyte help delay electrolyte degradation and dry-out throughout the cell.

5 Perspective on R2R system improvements and costs

5.1 Preemptive design of electrode microstructures

The work presented here used an existing electrode pair designed for automotive applications, which was not initially intended for laser ablation. We consider co-design and optimization of electrodes and their laser-ablated microstructures an area for substantial further performance gains. For example, the electrodes used in this work were initially designed with an N/P ratio of 1.19, but in the laser-ablated case this was reduced to a sub-optimal value of 1.13. Ideally, the initial electrode loading after coating would compensate for the anticipated mass removal, such that after ablation the target N/P ratio of 1.19 is achieved for the laser-ablated system. Further, the porous microstructure for these electrodes was optimized for non-ablated cells. Better performance for laser-ablated cells could be achieved by co-optimizing the electrode microstructure and laser-ablated pattern. Consider an anode consisting of plate-like particles oriented parallel to the current collector. In this case, the in-plane tortuosity is significantly lower than the through-plane tortuosity. Here, laser ablation could open through-plane diffusion pathways, which subsequently access the favorable in-plane diffusion pathways, resulting in a more homogeneously utilized electrode. The porosity of such an anode could be significantly reduced without much impact on the average Li-ion tortuosity, while increasing the cell's volumetric energy density. When scaling to manufacturing production facilities, further optimization and strategic design of electrode coatings that pre-empt the ablated geometries is encouraged but is beyond the present work's resources.

5.2 Techno-economic analysis

A cost-model was developed using the BatPaC modeling software[56] for incorporating laser ablation into a production-scale R2R line. The cost-model assumes a large scale production plant of 50 MWh/year producing cells with a 4 mAh cm^{-2} NMC811 cathode paired with a graphite anode with an N/P ratio of 1.2. In addition to the baseline production costs outlined on the BatPaC webpage,[56] the analysis incorporates capital expenses for the laser and additional floor space, as well as ongoing costs for laser maintenance, increased power consumption, and extra material required for the laser-ablated anode.

To explore the impact of the various changes to production cost, the following costs were added in a step-wise sequence, *e.g.*, step 4 includes the costs from Steps 1–3 *etc.*:

1. Baseline production costs from the BatPaC software model (*i.e.*, no change).

2. 6% anode material is ablated and assumed to be lost and unrecoverable. $10 per kg was assumed for the graphite cost.

3. The porosity of the remaining anode is increased from 25% to 30%.

4. The porosity is further increased from 30% to 35%.

5. The additional capital expense of the laser infrastructure amounts to $3M.

6. The total additional capital expense amounts to $5M.

7. Laser-ablated channels reduce the electrolyte filling time by 85%.

Fig. 12 shows the cost summary. The greatest impact to the production cost stems from the material lost during laser ablation and any increase in porosity on the remaining anode.

However, the material-loss cost is highly conservative considering that previous work has shown that ablated materials can be directly recovered and recycled or, in the case of graphite, be directly re-incorporated into a new slurry.[21] Thus, we expect substantially lowered associated material-loss costs if such recycling methods are implemented. However, the cost-model for material recovery and reuse is beyond the scope of this work. When considering the expenses associated with capital, additional maintenance, and additional floor space, there is only a marginal change in production cost of around $0.02 per kWh. Additionally, there is anticipated cost reduction from accelerating the electrolyte filling step. For example, in Step 7 it was assumed that the time for filling and soaking could be decreased by 85%, which is estimated to save $0.18 per kWh.

Overall, the production cost, while mostly attributed to loss of anode material, came to ≈$1.31 per kWh. This estimate is lower than the $1.96 estimated by Hille *et al.*,[33] for a production facility located in Germany where many expenses like labor, construction, and capital were considerably different than those used for the BatPaC model, which assumes construction and operation in the United States.

5.3 R2R system design

A number of lessons were learned during the pilot scale demonstration presented in the present manuscript. Prominently, the debris extraction system design presented here was inadequate to handle the volume of post-ablation debris produced. The poor performance may be primarily attributed to the following:

1. The case fans provided a poorly directed, turbulent, and relatively low-velocity airflow. Turbulence helped to spread the debris across a wider area including both away from the vacuum inlet and towards the laser optics.

2. The flow produced by the fans was not directed directly towards the inlet of the vacuum system, further reducing its collection efficiency (*i.e.*, the fan and inlet axes were orthogonal).

3. Debris particle sizes were larger and heavier than expected causing them to quickly fall out of suspension.

4. The vacuum system did not generate adequate flow to capture the unexpected large-particle debris.

To address these issues, the laser and optics should be isolated from the electrode ablation to prevent fouling and subsequent damage. The downstream face of the f-theta lens (often protected by a glass window) will then be the only optic exposed to post-ablation debris. Further, if this optic is downward facing, then no fouling is expected, precluding a dedicated lens cleaning system. Such a setup could also be fitted with filtered ventilation to prevent dust accumulation in the optics compartment, reducing the frequency of optics maintenance. Fig. 13 shows these improved design principles on a hypothetical setup diagram.

We suggest that future R2R laser-ablation systems employ a more aggressive and highly engineered airflow to remove ablation debris. Such a system should use a high-velocity laminar gas flow (*e.g.*, an air knife), which is directed directly towards a high-flow

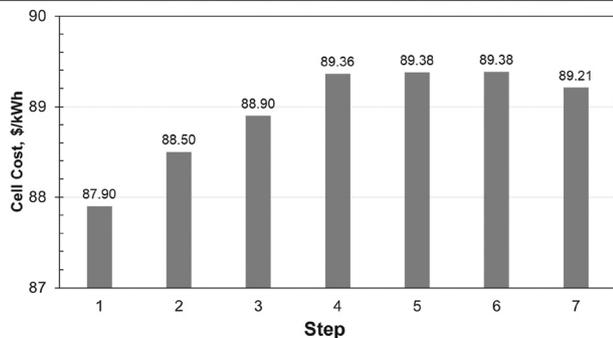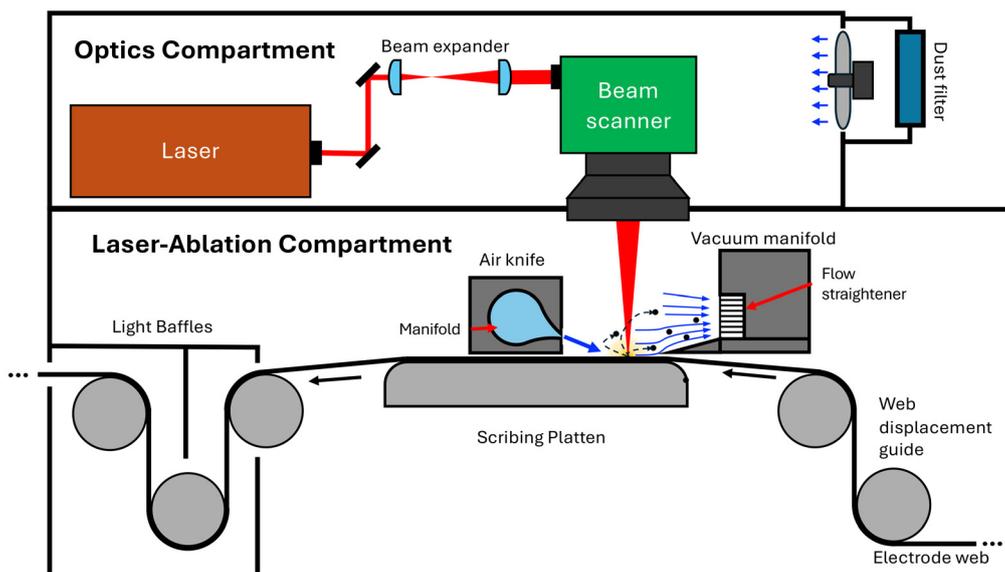| Step	1	2	3	4	5	6	7
Laser Ablation, %	0	6	6	6	6	6	6
Anode Porosity, %	25	25	30	35	35	35	35
Negative Coater							
Labor, hours/year	54,233	54,233	54,211	54,187	56,430	56,430	54,430
Capital, M$	90	90	90	90	93	95	95
Area, sq.m.	19,431	19,431	19,420	19,408	19,420	19,420	19,420
Electrolyte Filling							
Labor, hours/year					125,700	125,700	18,000
Capital, M$					24.9	24.9	3.6
Output							
Cell Cost, $/kWh	87.90	88.50	88.90	89.36	89.38	89.38	89.20
Difference in Cell Cost, $/kWh		+0.60	+0.40	+0.46	+0.01	+0.01	-0.18
Cumulative Diff. in Cell Cost, $/kWH							+1.31

Fig. 12 Table showing the effect various process parameters have on manufacturing cost and a bar chart visualization.

Fig. 13 Schematic of an ultrafast laser–ablation system for processing a battery electrode on a R2R machine incorporating lessons learned from the pilot demonstration.

vacuum system. Subsequently, a cyclone separator, or similar, should be used to collect debris for reuse or recycling.[21] Such a redesigned system is expected to prevent electrode contamination, reduce costs associated with material loss, and reduce the energy costs associated with filtering file particulates from air-flows.[57] Further, if there is additional risk of contamination of electrodes with ablation debris, soft bristled brushes can also effectively be used to clear away debris.

Another challenge was the misalignment of the laser pattern on the electrode web surface during the initial meters of processing. In the future, employing a web displacement guide immediately before the laser-ablation optics will likely eliminate most, if not all, of the misalignment. Throughput can also be improved with better alignment because less overshoot of the laser pattern on either side of the electrode coating will be required to accommodate web drift. Further, web-edge detection at the ablation location or in-line smart image processing to detect the electrode coating can be used to adjust the pattern location in real time, depending on the beam-scanning architecture.

6 Scaling throughput to 50 m min⁻¹

The R2R ultrafast laser-ablation process must be scaled to state-of-the-art industrial processing speeds to prevent manufacturing bottlenecks and make laser-ablated electrodes cost-competitive. This section will discuss various options and strategies to scale laser processing to a benchmark throughput of 50 m min^{-1}. Single-sided processing is assumed, though the optical system can be doubled if double-sided processing is desired.

For high-throughput analysis, we will consider processing a single-side of roughly the same electrode used in the experi-

mental portion of this manuscript. Hence, requiring an ablated width of 120 mm and a graphite coating thickness of 80 μm. Because there is diminished benefit from ablating more than half the thickness of the electrode,[52,53] we target a 40 μm pore depth, and a pore-to-pore center spacing of 100 μm to achieve reasonably good fast-charge performance and active-material utilization. The pores are assumed to be hexagonally arranged. We will target a typical pore diameter of 30 μm, which can be achieved with a focused spot size of ≈20 μm (note that graphite features generally ablate larger than the focused laser spot-size).[19,20,24]

The laser(s) used for this hypothetical scenario will be one of the emerging kW class of industrial ultrafast lasers. As such, we will assume a laser with a time-averaged power of 1 kW, and a 100 μJ pulse energy, and a pulse duration of ≤600 fs. The latter two specifications are comparable to current commercially available Yb:YAG femtosecond lasers. Such a laser would have an f_{rep} of 10 MHz and center wavelength near 1030 nm. Ablation characterization of graphite electrodes by Tancin *et al.*[20] and Habedank *et al.*[11] indicated that with these laser parameters, we can expect that it would take ≈6 laser pulses to ablate one of these pores at a local repetition rate (f_{local}, the frequency of laser pulses incident on a single feature) ≤10 kHz. For high process throughput, multiple lasers may be employed. More powerful lasers will likely become available in the future, though this may not be desirable if the higher powered lasers require exotic optical solutions such as water-cooled mirrors to prevent thermal damage.

6.1 Constraints and considerations

Generally, the maximum possible system throughput is determined by (1) the required mass removal to achieve the desired microstructure and (2) the rate that material can be removed

by the laser's delivered optical power. Noting that the material removal rate is affected by geometric constraints (*e.g.*, lower ablation efficiency when ablating the bottom of a deep, high-aspect ratio feature) shielding (*i.e*, absorption, reflection or scattering of a laser pulse by the plume or debris produced by the previous pulse(s)), and laser-energy utilization (the percent time the laser is actively ablating the electrode).

First, the material removed per pulse generally decreases as a feature gets deeper.[20] For example, similar performance for less material removal may be achieved by reducing the pore diameter for a high-rate optimized electrode. However, this may cause an intolerable reduction in throughput, and hence should be considered when choosing a target microstructure. Modeling indicates that there is diminishing benefit to high-rate performance from ablating to a depth of more than half the thickness of the electrode.[52,53] Lower process throughput and higher costs associated with greater material loss may make half-thickness feature depths a soft limit in commercial applications.

Second, throughput is maximized when the optical energy required to create a feature is minimized. In other words, throughput is maximized when shielding is minimized. There are two types of shielding relevant to electrode ablation: plasma shielding and particle shielding. Plasma shielding occurs when an ultrashort light pulse generates an electron–hole plasma, typically when fluence is much higher than the ablation-threshold fluence.[58] Shielding occurs when the plasma is ejected from the microstructure and blocks or perturbs subsequent laser pulses,[24,59–62] while often conducting thermal energy back to the substrate.[62] Alternatively, particle shielding is potentially more problematic compared to plasma shielding since during ultrafast laser-ablation, whole or fragments of particles are ejected from the electrode sheet as the binder constraining the active material particles is vaporized more readily than the particles themselves.[5,9,21,24,63] Thermal buildup can also occur because ≈30% of the incident laser energy remains in the substrate as heat after ablated material ejection.[64,65] Thermal buildup is exacerbated at high-pulse repetition rates because there is insufficient time to dissipate heat into the bulk material.[60,62,66–71] Thus, high-quality microstructures can be created at scale by limiting shielding and thermal buildup.[72] Limiting shielding and thermal buildup requires limiting either the pulse repetition frequency or the overlap time of subsequent pulses at the same location. To achieve the same amount time-average power, the pulse repetition frequency f_{rep} can be reduced if the pulse energy is similarly increased. However, increasing the pulse energy is not currently feasible for industrially relevant short-pulse lasers because beyond the low-100s of μJ, peak power levels inside the laser requires more complex and expensive optics to manage undesirable nonlinear effects and laser-induced damage to optical components.[37,61,73] Hence, optical system designs need to allow for fast-beam scanning to reduce pulse overlap at high repetition-frequencies.

6.2 Optical system design

The power and pulse-energy requirements discussed earlier are quoted at the laser's exit aperture. However, various optics are needed to direct and manipulate the laser beam before it is incident onto the electrode surface, which all contribute some loss of power. Conservatively, we estimate that 8 mirrors are required to direct the laser beam and scan it across the electrode surface. Ultrafast-laser mirrors with low group-delay dispersion (GDD) and reflectivities ≥ 99.5% are readily available for Nd:YAG and Yb:YAG laser fundamental wavelengths. Further, exit aperture beam sizes are typically ≤5 mm. So, a beam expander is needed to enlarge the beam such that a final scanning lens can focus the laser beam to a sufficiently small spot size. Both of these lens-systems likely have tranmissions of ≥99.5%. Furthermore, certain electro-optic and acousto-optic devices (discussed in section 6.3.4) may be incorporated into the optical setup, of which, acousto-optic devices have transmission near 95%. Summing these losses, we can assume that ≈90% of the pulse energy available at the laser aperture is available for ablation.

Next, selecting an appropriate scanning lens is essential to obtain realistic lens properties, including maximum aperture, scan area dimensions, focal length, and working distance. Searching the available lenses on the market, the f-100K-10-1064 f-theta lens offered by Von Jan Technology offers a 10 mm maximum beam size, 100 mm focal length, working distance of 106 mm, and scan area diameter of 99 mm, which has appropriate properties for this application. A beam expander will be used to achieve a beam diameter of 8 mm with a beam quality factor (M^2) of 1.2.

6.3 Galvo-scanners

Galvo-scanners are ubiquitous for laser beam scanning for many bench-top laser scribing and marking systems. However, they cannot provide adequate scanning speeds to maintain adequate pulse-to-pulse separation for high-repetition-rate lasers. Further, with small angle response times typically in the range of 100s of μs, they are also unable to ablate pores feature by feature without unacceptable losses to laser utilization.

6.3.1 Polygon-scanners. Polygon scanners are of interest for laser microstructuring at industrially relevant throughputs because they excel at providing high, uni-directional beam-deflection angles and deflection speeds.[37–40,72,74–76] By rotating at a constant speed, these scanners avoid the inertial limitations that plague systems that rely on moving mirrors with servos or MEMS devices. Further, the laser beam moves across the surface of the polygon wheel as it rotates, spreading the thermal load while the high tangential speeds provide cooling airflow, both of which mitigate damage from thermal buildup. Because the beam is scanned in a single direction, maximum time is allowed for debris removal before the next laser pulse arrives. A survey of polygon scanner manufacturers conducted by Römer *et al.*[76] determined approximate upper performance limits for these devices, which include input beam diameters of 12 mm, deflection angles up to ±1 rad (±57°), and deflection rates of 10 000 rad s^{-1}. A system designed with a polygon scanner uses the polygon wheel to scan the laser beam in the *x*-direction, while a galvo-controlled mirror or solid-state optical deflector (see section 6.3.4) is used to compensate for

the electrode web motion and advance the laser spot forward to the next pattern row.

Designing or choosing a polygon scanner for a given application is a complex process compared to using other scanning systems. When selecting an appropriate polygon scanner, two design considerations are vignetting and scan-field distribution asymmetry effects. Vignetting is the effect of having a fraction of the total laser beam being reflected from a polygon-scanner facet as the beam moves from one facet to the next when rotating the polygon. It is undesirable to use the laser light when vignetting occurs because electrode features will be unevenly ablated (see Li,[74] Chapter 3, Fig. 3.8). The percentage of the scan angle affected by vignetting can be reduced by reducing the number of facets (sacrificing scans per second), reducing the beam size (sacrificing focused laser spot size), or making the polygon wheel larger (sacrificing packaging and, potentially, max rotational speed). For this reason, polygon scanners generally do not accommodate beam diameters larger than around 10–12 mm. Scan-field distribution asymmetry refers to changes in the beam-scanning speed caused by the reflecting point changing as the polygon rotates. Greater deviation from the average scan-rate occurs at either end of the scanning angle. For cases where a multi-pass strategy is implemented, pore-to-pore spacing can potentially vary widely across the scan, resulting in uneven feature spacing across the electrode. Scan-field distribution asymmetry can be reduced by altering the input beam angle but only to the point where the incident and reflected beams maintain adequate separation to allow space for the scan lens. These parameters are also coupled with the parameters that govern beam vignetting. Numerous other considerations also effect the usable scan angle. Generally, only ≈60% of the scan angle is usable,[74] which is reflected in the subsequent design calculations. The usable fraction of the total scan, or scan utility, is denoted as η.

With the chosen scan lens, the required beam deflection θ (in radians) to scan across a specified electrode width w electrode can be expressed as

$$\theta = \frac{w}{2F}, \tag{1}$$

where F is the f-theta lens' effective focal length. Knowing the laser's f_{rep} and the desired scanning width w, the scan frequency f_{scan} (in scans per s) can be represented as

$$f_{scan} = \frac{f_{rep}\eta d}{w}, \tag{2}$$

where d is the pore-to-pore spacing. Further, eqn (2) can be modified to yield the polygon wheel revolutions per minute (RPM) for a given number of facets by multiplying by 60 and dividing by the number of facets (N_{facet}), yielding

$$RPM = \frac{60 f_{rep}\eta d}{w N_{facet}}. \tag{3}$$

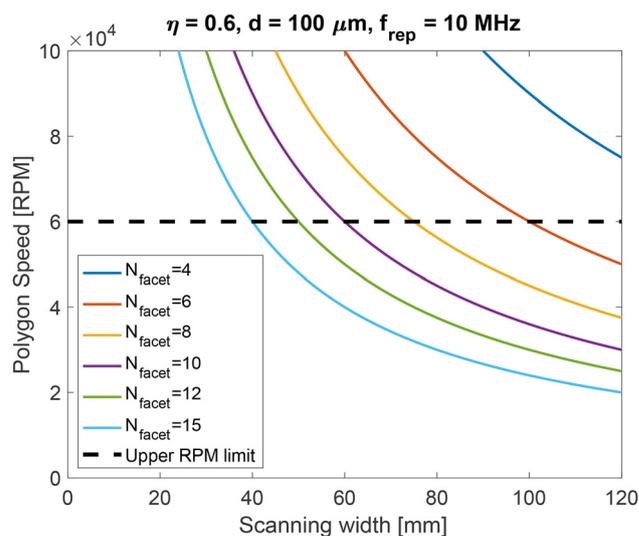Fig. 14 shows a diagram where the required polygon wheel RPM is plotted against the scanning width for wells with

Fig. 14 Required polygon wheel RPM to achieve 10 000 scans per s as well as the associated maximum scanning width.

different N_{facet}. Polygon scanners are best operated within the range of 60 to 60 000 rpm. Below 60 rpm, speed and positional control can become complicated and above 60 000 rpm, the motor efficiency suffers, requiring more sophisticated bearings.[75] From Fig. 14, assuming a scan utility of η = 0.6, an assumed pore-to-pore spacing of d = 100 μm, and a repetition rate of f_{rep} = 10 mHz, a polygon wheel must have at least 6 facets to achieve less than 60 000 rpm. From the selected f-theta lens, the maximum scanning width is w ≈ 80 mm, further limiting the facet number to $N_{facet} \geq 10$. For the present study a scan width of w = 60 mm is selected to allow for two equal scanning systems to act in parallel on either side of the electrode web. Using eqn (1) the optical deflection half angle of $\theta/2$ = 0.3 rad (17.2°) is needed. Assuming that only 60% of the optical scanning angle is usable, the total optical deflection angle θ of 1 rad (57.3°) is needed. The max possible deflection angle of a polygon scanner θ_{max} is[75]

$$\theta_{max} = \frac{720}{N_{facet}}. \tag{4}$$

From this constraint, the maximum number of facets that satisfies the required beam deflection is $N_{facet,min}$ = 12.57, meaning that $N_{facet} \leq 12$. Using the above constraints of maximum RPM and maximum possible deflection angles, a polygon with 10–12 facets is appropriate for this application. For the purposes of this study, a polygon with 12 facets is selected, which corresponds to required wheel speed of 50 000 rpm.

Next, the maximum material throughput (*i.e.*, the web speed) can be calculated using the assumed hexagonal pattern and specified laser-system constraints. Since the pores are hexagonally oriented, the row-to-row spacing (in the y-dimension)

is related to the pore-to-pore spacing as $0.866d$. Thus the system throughput T (in m min^{-1}) is given by

$$T = \frac{0.866d^2 \eta f_{rep}}{w}\left(\frac{60}{1000}\right). \quad (5)$$

Eqn (5) yields a throughput of 8.66 m min^{-1} for two laser and scanning systems processing in parallel, well short of the 50 m min^{-1} goal. To achieve 50 m min^{-1}, 12× laser/scanning systems need to be used, (6 lasers in series for each half of the electrode), yielding a final processing throughput of $T = 52$ m min^{-1}. Importantly, the number of laser/scanning systems must be even because the phase of the pattern in each subsequent row is shifted 180° in phase from the previous row. This configuration is illustrated in Fig. 15 with some modifications discussed later in section 6.3.4 that uses a hybrid scanning system to reduce the number of required lasers by half.

A final consideration is the need to compensate for the electrode web velocity during scanning, and after a row of pores is completed, advancing to the next row to be ablated. For this example, moving 6 rows forwards corresponds to 520 μm (or 0.0052 radians with the chosen f-theta lens). This is ideally accomplished within the 40% of downtime between scans, which is unusable due to vignetting or scan field distribution asymmetry (i.e., within ≈40 μs). Typical small-angle step response times for high-performance galvo scanners are on the order of low 100s of μs meaning that, at minimum, a scan-

ning row could be lost when waiting for the mirror to move, reducing throughput by over 15%. Acousto- or electro-optic beam deflectors (discussed in detail in section 6.3.4) are a possible solution to avoid additional processing downtime. An elegant solution is to employ an irregular polygon wheel, meaning that each facet of the polygon is tilted slightly in the y-direction to move the beam in the y-dimension to account for the web motion and advance the beam to the next pore row. Notably, this solution only works if N_{facet} is an integer multiple of the number of pulses needed to ablate each pore.

6.3.2 Diffractive optical elements. Another solution for achieving high laser-ablation throughput is to use diffractive optical elements (DOEs). Microstructures on the surface of these optics diffract light, deflecting it into precise shapes, for example, a 5 × 5 spot matrix. In such a configuration, a single laser beam can be used to ablate 25 pore features simultaneously. The advantage of this method is that multiple features can be ablated in parallel without needing to scan the laser beam. This can be an advantage for relatively slow scanning systems like galvo-scanners because, in this example, the time loss to scanning is effectively reduced by a factor of 25. However, because each laser pulse is split 25 ways, the pulse energy incident on an individual feature is also reduced by a factor of 25, and a proportionally larger number of pulses will be needed to create the desired microstructure. However, this can also be seen as an advantage when the full laser power of an un-split beam is excessive for ablating a single feature. In
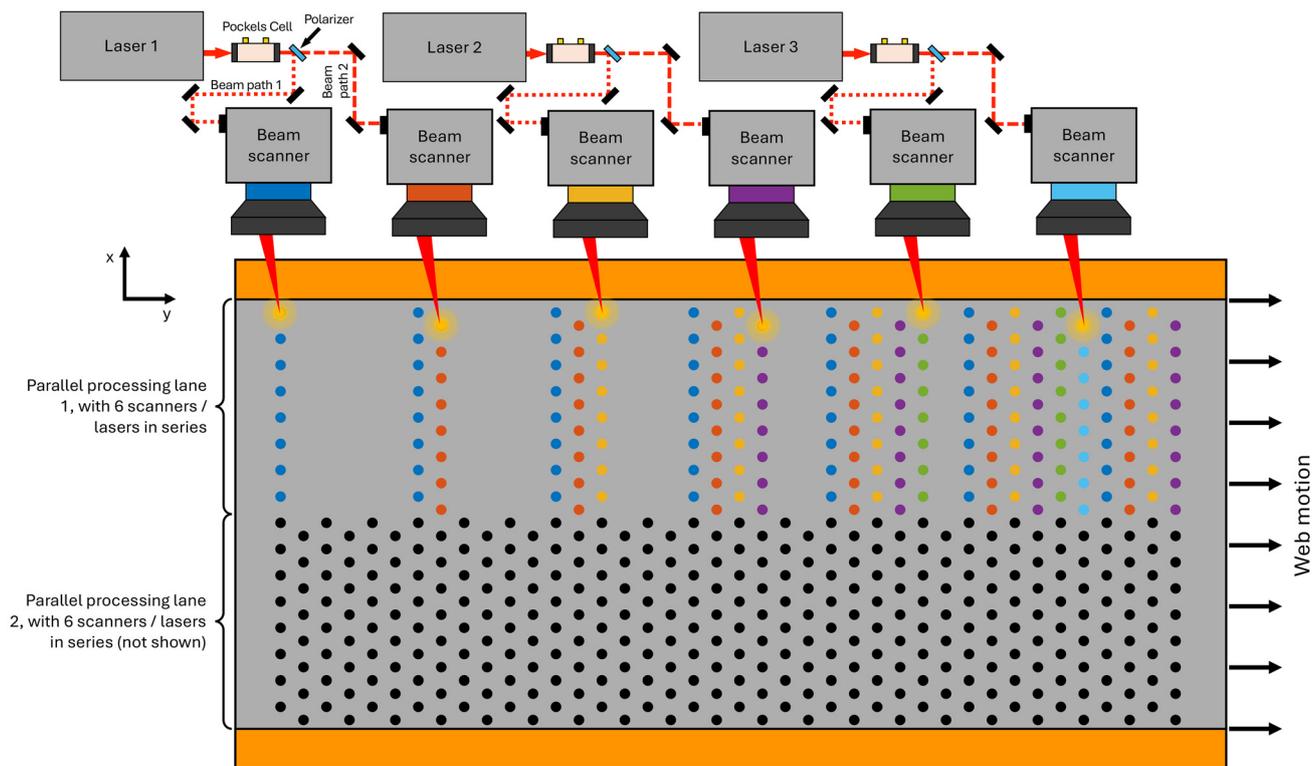
Fig. 15 Layout of optical setup with 6 scanners in series and another 6 in parallel. This setup demonstrates the use of Pockels cells as fast optical switches to enable 100% laser utilization by switching the laser beam between two scanners, which is discussed in detail in section 6.3.4.

this configuration, f_{local} will be equal to f_{rep} for each pore, risking potential thermal buildup in the electrode and shielding-induced loss of feature resolution. We believe that faster scanning solutions (*e.g.*, polygon and resonant scanners) which enable adequate spatiotemporal separation of laser pulses are preferable.

6.3.3 Resonant scanners. Another option for beam scanning is using a resonant scanner. A resonant scanner employs a mirror fixed to a spring such that the mirror oscillates angularly at its resonant frequency. The mirror mass and spring stiffness can be adjusted to change the mirror's resonant frequency to achieve a desired scanning rate. Scanners are available at rates up to 16 kHz (RR = 32 000 scans per s),[77] with typical optical deflection angles in the low 10s of degrees, which is suitable for multi-pass processing. These systems also contain few to no wearing parts and have a surprisingly high tolerance to external vibrations from, for example, other machinery. Further, resonant scanners require much less system design than polygon scanners, with the resonant frequency and beam diameter being the only two major parameters.

A drawback of the resonant scanning system is its intrinsically sinusoidal motion, which causes the feature spacing on the electrode to vary accordingly. This sinusoidal constraint can be somewhat accounted for by using only the middle 50% of a given scan, which best approximates linearity, as shown in Fig. 16. Fig. 16c demonstrates that across the usable scanning angle, an average pore-to-pore spacing of 100 μm can be obtained, with the local pore-to-pore spacing ranging from 82 μm to 110 μm at the edges and center, respectively. This variance may be an acceptable drawback in exchange for the reducing system cost, complexity, and required maintenance. It is worth noting that specialized optics can be used to linearize much of the sinusoidal scan, such as convex elliptical mirrors[78] and refractive-diffractive optics.[79,80] Employing these optics can improve the usable range from 50% to ≈70–80% of the scan, increase the maximum deflection angles, and improve the uniformity of pore-to-pore spacing across the usable scan range. Like with polygon scanners, this system can also incorporate a galvo-scanning mirror for web-motion compensation in the *y*-direction.

6.3.4 Solid-state optics and hybrid scanning systems. Solid-state optics have utility in industrial laser ablation applications as both fast beam deflectors and optical switches. With no moving parts, they are exceedingly reliable and require little to no maintenance, making them ideal for applications sensitive to cost and system downtime. Further, power consumption is minimal compared to the laser's power requirements. Acousto- and electro-optic beam deflectors (AODs and EODs, respectively) are optical solid-state deflectors that excel at extremely fast and accurate beam deflection, typically at the expense at smaller deflection angles when compared to mirror-based scanners.

AODs typically utilize a piezoelectric crystal to produce a sound wave that propagates through an optical crystal, inducing a periodic change in the crystal's refractive index. This
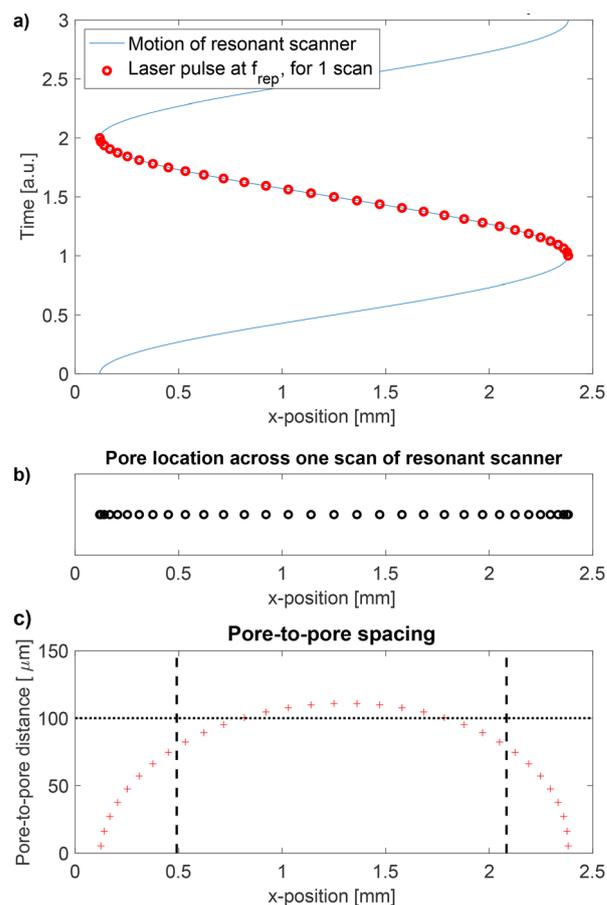
Fig. 16 (a) *X*-Position of a resonant scanner as a function of time, with pulse locations for a laser of arbitrary rep rate for illustration of pattern distortion. (b) Pore locations for a single scan illustrating the effects of nonlinear scanning. (c) The distance between adjacent pores with dotted line showing the average pore-to-pore distance across the usable portion of the scan (denoted by the dashed lines).

periodic change in refractive index change causes the crystal to act as a diffraction grating, producing multiple orders of diffraction. If the input beam's angle of incidence is at the Bragg angle, the beam will be efficiently deflected by the first-order diffraction with higher orders being suppressed. Changing the acoustic frequency (and therefore the grating spacing) subsequently changes the beam deflection angle. However, greater deflection angles increasingly deviate from the Bragg condition resulting in decreased diffraction efficiency (*i.e.*, increased power loss to the zeroth-order diffraction). Typically, the maximum deflection angle of an AOM is determined as the angle where efficiency of the first-order diffraction falls to ≈50–60%.[76,81] Scanning speeds of up to 250 000 rad s^{-1} are possible, and the deflection bandwidth is limited by the speed at which a new acoustic wave can propagate across the incident beam diameter. Hence, the scanning bandwidth is proportional to the speed of sound in the crystal and inversely proportional to input beam diameter. While AODs can accept input bean sizes up to 10 mm in diameter, a maximum deflec-

tion angle of 0.05 rad make these scanners impractical as a sole beam scanner in these applications.

EODs utilize an electric-field-induced gradient in the refractive index to steer the laser beam using the optical Kerr effect. These devices have similar deflection speeds as AOMs, while maintaining higher throughput efficiency (usually >90% irregardless of deflection angle) and max deflection angles of 0.2 rad. The bandwidth is limited only by the ability of the voltage driver to overcome the EOD capacitance. Further, quadrupole EODs have been demonstrated, which can deflect the beam in x- and y-axes simultaneously using a single device.[82] However, these devices currently only accept input beams of ≤3 mm, severely limiting the minimum laser spot-size unless a lens with a very short focal length is used. For an EOD to be used as the sole beam scanning device, a 32 mm focal length lens is needed to achieve a spot size near 30 μm, resulting in a scan width of only 6.4 mm, making this setup impractical for the current application.

Finally, electro-optic modulators, such as Pockels cells can be used as a fast optical switch to direct selected pulses along alternate beam paths. For example, a Pockels cell can be operated as a controllable half-wave plate to rotate the polarization of selected pulses. Thus, a subsequent polarizer can either transmit a pulse along one beam path or reflect it to another depending on whether the Pockels cell has altered the polarization.

The true utility of solid-state optics is the ability to integrate with a fast mirror-based scanner to create a hybrid scanning-system. Numerous examples exist in the literature of augmenting mirror-based scanners with fast EODs or AODs to achieve a "best of both worlds" performance of both high scanning speeds and deflection angles. Matsumoto *et al.*[83] incorporated a pair of x- and y-axis-oriented AODs to augment a dual-axis galvo scanner. The AODs allowed for higher peak acceleration of the laser spot when navigating sharp corners, by using the AODs to correct for errors such as overshoot caused by the mirrors' inertia. Further, they demonstrated that the AODs can be used to achieve pule-to-pulse separation or multi-row processing for high repetition rate lasers (f_{rep} ≥ 2 MHz).[73,83,84]

In the previous sections where polygon and resonant scanners were discussed, typical processing conditions required these scanners to be operated at the upper end of speed, beam size, and deflection angles, which may increase their initial cost as well as increase the maintenance and downtime requirements. Integrating AOD or EODs can mitigate some of these challenges. For example, the width-wise scanning speed can be reduced by half if a fast AOD or EOD is used for small angle deflection of every other pulse in the y-dimension, allowing for two rows of pores to be ablated simultaneously. In addition to reducing the speed or deflection angle requirements by a factor of two, a single laser can now ablate both 0° and 180° phase pore patterns, eliminating the need to have a even number of lasers.

In the case where polygon or resonant scanners are employed for fast x-direction scanning, ≈50% of the scan may be unsuitable for laser ablation (see Fig. 14c). If two scanners are synchronized such that their scans are 180° out of phase, a Pockels cell can be used to direct pulses to one scanner or another depending on which is in its usable scanning range. Thus, 100% of the available laser power can be used for ablation. Fig. 15 illustrates the a laser-ablation system using a hybrid scanner/Pockels cell system.

Finally, section 6.3.1 discusses the available time to advance the laser spot to the next pattern row. As alluded to previously, EODs or AOD present an ideal solution for advancing the laser spot to the next row within the available scanning downtime.

7 Conclusions

In this work, we successfully integrated an ultrafast laser and galvo-based scanning optics into a R2R processing machine and subsequently completed a pilot-scale demonstration of microstructuring 2 sides of a 700 m long graphite anode. The laser integration was accomplished with minimal modification of the R2R machine. Both sides of the electrode were patterned with a hybrid microstucture designed for the dual optimization of fast-charging and fast wetting. Subsequently these electrodes were paired with an NMC-111 cathode and manufactured into prismatic cells with 27 Ah capacity, a first for laser-structured electrodes in terms of both capacity and format. The 27 Ah cells demonstrated superior soaking time having achieved a greater capacity during formation after 2 hours of soaking as non-ablated cells did after 5 hours. The laser ablated cells demonstrated superior fast charging benefit achieving >30% capacity acceptance during 6C charging for several cycles, and being able to maintain continuous 4C charging for over 100 cycles with significantly lower rate of capacity fade than non-ablated cells. Finally, the laser ablated cells demonstrated superior cycle life at 0.5C cycling, having reached >2800 cycles without any cells experiencing the capacity fade "knee" at end-of-life while 8 out of 9 non-ablated cells experienced the "knee" by 2200 cycles, therefore a life-extension of >40% is achieved. While the scope of this work did not allow these cells to be continuously cycled until all cells failed, other work from the literature suggests that laser ablated cells may last 3–4× longer than their non-ablated counterparts.

Further, we provide a perspective on the adoption of this technology by industry, specifically, in terms of economic costs, pre-emptive electrode design, and scalability. Our techno-economic analysis concluded that only a marginal increase of $0.02 per kWh in production cost is expected for a 50 MWh per year production facility. We also believe that the performance benefits realized in this work can be substantially improved upon by (1) using a more optimized, coupled laser-ablated microstructure, (2) implementing systems for better pattern control, and consistency (*e.g.*, larger than optimal pore-to-pore spacing and pronounced row-to-row spacing variability were realized in this study), and (3) integrated electrode design. Integrated electrode design includes compensating the

cathode electrode loading to account for the ablated subsequent active-material mass removal from laser ablation. We discussed the shortcomings of our system design and provide suggestions for future improvements. Particularly, the management of optic fouling and the optical compartment design can be greatly improved.

Finally, an hypothetical system was proposed and analyzed to suggest that this technology is ready to achieve state-of-the-art process speeds up to 50 m min^{-1}. The hypothetical system is composed of a high-power ultrafast laser, of the emerging kW-class industrial ultrafast lasers that will almost certainty have a near-infrared wavelength. Optical losses throughout the system from beam expenders and mirrors that can be kept under 5% with pulse duration preserved, achieved by using high-quality optics designed for ultrafast lasers. A fast mirror based scanner, including either a polygon scanner or resonant scanner, is suggested to be an ideal choice for high-speed x-axis scanning to keep f_{local} sufficiently low. We strongly recommend a hybrid scanning system that employs a combination of AODs, EODs, or Pockels cells. AODs and EODs can be used to advance the laser to the next pattern row and/or ablate multiple pattern rows simultaneously, reducing the fast-scanning requirements. Pockels cell are suggested to be introduced to act as a fast optical-switch to alternate the beam path between two scanners to utilize 100% of the available laser power (excluding a small additional transmission loss through the Pockels cell), doubling the potential throughput for a given number of lasers. The main takeaway from this analysis is that scanning systems, using currently available technology, are more than capable of keeping up with start-of-the-art web speeds.[37] While commercially available "plug-and-play" systems (*e.g.*, dual-axis galvos) generally fall short in terms of the required capability, the laser-scanning technology field is broad and complex, and designing a custom beam scanning system with vastly superior performance can be readily accomplished, enabling fast and economic laser structuring of li-ion battery electrodes.

Author contributions

Ryan J. Tancin: methodology development, experimental construction and investigation, data analysis, throughput modeling and analysis, original manuscript preparation, manuscript review and editing Bertan Özdoğru: cell building, electrochemical data analysis Nathaniel Sunderlin: electrochemical data analysis Peter J. Weddle: software development, manuscript review and editing, Francois L. E. Usseglio-Viretta: software development, data curation David R. Boone: call building, electrochemical test design, and data analysis Quentin Mocaer: laser and optics supplier and technical support Eric Audouard: laser and optics supplier and technical support Kevin W. Knehr: techno-economic analysis, manuscript review and editing Joseph J. Kubal: techno-economic analysis, manuscript review and editing Shabbir Ahmed: techno-economic analysis, manuscript review and editing Donal P. Finegan:

project conceptualization, funding acquisition, project supervision, methodology development, manuscript review and editing Bertrand J. Tremolet de Villers: project conceptualization, funding acquisition, project supervision, methodology development, manuscript review and editing.

Conflicts of interest

There are no conflicts to declare.

Data availability

The data that support the findings of this study are available from the corresponding author upon reasonable request.

Acknowledgements

References

1 W. Sibbett, A. Lagatsky and C. Brown, *Opt. Express*, 2012, **20**, 6989–7001.

2 S. Lei, X. Zhao, X. Yu, A. Hu, S. Vukelic, M. B. Jun, H.-E. Joe, Y. L. Yao and Y. C. Shin, *J. Manuf. Sci. Eng.*, 2020, **142**, 031005.

3 F. Dausinger, F. Lichtner and H. Lubatschowski, *Femtosecond technology for technical and medical applications*, Springer Science & Business Media, 2004, vol. 96.

4 J. Pröll, B. Schmitz, A. Niemoeller, B. Robertz, M. Schäfer, M. Torge, P. Smyrek, H. Seifert and W. Pfleging, *Laser-based Micro-and Nanoprocessing IX*, 2015, pp. 329–335.

5 N. Dunlap, D. B. Sulas-Kern, P. J. Weddle, F. Usseglio-Viretta, P. Walker, P. Todd, D. Boone, A. M. Colclasure, K. Smith, B. J. T. de Villers, *et al.*, *J. Power Sources*, 2022, **537**, 231464.

6 J. Park, S. Hyeon, S. Jeong and H.-J. Kim, *J. Ind. Eng. Chem.*, 2019, **70**, 178–185.

7 J. Park, C. Jeon, W. Kim, S.-J. Bong, S. Jeong and H.-J. Kim, *J. Power Sources*, 2021, **482**, 228948.

8 J. B. Habedank, F. J. Günter, N. Billot, R. Gilles, T. Neuwirth, G. Reinhart and M. F. Zaeh, *Int. J. Adv. Des. Manuf. Technol.*, 2019, **102**, 2769–2778.

9 W. Pfleging, R. Kohler and J. Pröll, *Laser-Based Micro-and Nanoprocessing VIII*, 2014, pp. 57–64.

10 W. Pfleging and J. Pröll, *J. Mater. Chem. A*, 2014, **2**, 14918–14926.

11 J. B. Habedank, J. Endres, P. Schmitz, M. F. Zaeh and H. P. Huber, *J. Laser Appl.*, 2018, **30**(1–7), 032205.

12 J. W. Braithwaite, A. Gonzales, G. Nagasubramanian, S. J. Lucero, D. E. Peebles, J. A. Ohlhausen and W. R. Cieslak, *J. Electrochem. Soc.*, 1999, **146**, 448.

13 G. Vennam, A. Singh, A. R. Dunlop, S. Islam, P. J. Weddle, B. Y. W. Mak, R. Tancin, M. C. Evans, S. E. Trask, E. J. Dufek, *et al.*, *J. Power Sources*, 2025, **636**, 236566.

14 W. Pfleging, *Int. J. Extreme Manuf.*, 2020, **3**, 012002.

15 W. Pfleging, *Nanophotonics*, 2018, **7**, 549–573.

16 K.-H. Chen, M. J. Namkoong, V. Goel, C. Yang, S. Kazemiabnavi, S. Mortuza, E. Kazyak, J. Mazumder, K. Thornton, J. Sakamoto, *et al.*, *J. Power Sources*, 2020, **471**, 228475.

17 Y. Sterzl and W. Pfleging, *Batteries*, 2024, **10**, 160.

18 F. L. Usseglio-Viretta, P. J. Weddle, B. J. T. de Villers, N. Dunlap, D. Kern, K. Smith and D. P. Finegan, *J. Electrochem. Soc.*, 2023, **170**, 120506.

19 J. B. Habedank, J. Kriegler and M. F. Zaeh, *J. Electrochem. Soc.*, 2019, **166**, A3940.

20 R. J. Tancin, D. B. Sulas-Kern, F. L. Usseglio-Viretta, D. P. Finegan and B. J. T. de Villers, *J. Power Sources*, 2024, **596**, 234078.

21 R. J. Tancin, B. Özdoğru, N. S. Dutta, D. P. Finegan and B. J. T. de Villers, *J. Power Sources*, 2024, **596**, 234027.

22 F. Matsumoto, M. Yamada, M. Tsuta, S. Nakamura, N. Ando and N. Soma, *Int. J. Extreme Manuf.*, 2022, **5**, 012001.

23 E. Audouard, M. Fleureau, D. Pallarès, J.-M. Romano and F. Mermet, *Proc. CIRP*, 2024, **124**, 57–60.

24 A. Meyer, Y. Sterzl and W. Pfleging, *J. Laser Appl.*, 2023, **35**, 42036–42057.

25 M. X. Tran, P. Smyrek, J. Park, W. Pfleging and J. K. Lee, *Nanomaterials*, 2022, **12**, 3897.

26 P. Zhu, H. J. Seifert and W. Pfleging, *Appl. Sci.*, 2019, **9**, 4067.

27 Z. Song, P. Zhu, W. Pfleging and J. Sun, *Nanomaterials*, 2021, **11**, 2962.

28 J. Pröll, H. Kim, A. Piqué, H. Seifert and W. Pfleging, *J. Power Sources*, 2014, **255**, 116–124.

29 R. Kohler, P. Smyrek, S. Ulrich, M. Bruns, V. Trouillet, W. Pfleging, *et al.*, *J. Optoelectron. Adv. Mater.*, 2010, **12**, 547–552.

30 Y. Zheng, H. Seifert, H. Shi, Y. Zhang, C. Kübel and W. Pfleging, *Electrochim. Acta*, 2019, **317**, 502–508.

31 T. Tsuda, N. Ando, K. Matsubara, T. Tanabe, K. Itagaki, N. Soma, S. Nakamura, N. Hayashi, T. Gunji, T. Ohsaka, *et al.*, *Electrochim. Acta*, 2018, **291**, 267–277.

32 T. Watanabe, T. Gunji, T. Tsuda, F. Ando, N. Ando, S. Nakamura, N. Hayashi, N. Soma and F. Matsumoto, *ECS Trans.*, 2020, **97**, 859.

33 L. Hille, J. Kriegler, A. Oehler, M. Chaja, S. Wagner and M. F. Zaeh, *J. Laser Appl.*, 2023, **35**, 42054–42066.

34 A. Meyer, Y. Sterzl, S. Xiao, U. Rädel and W. Pfleging, *Laser-based Micro-and Nanoprocessing XVI*, 2022, pp. 123–132.

35 A. Meyer, P. Zhu, A. Smith and W. Pfleging, *Batteries*, 2023, **9**, 548.

36 A. P. Meyer, Y. Sterzl, U. Rädel, S. Xiao, M. Zenz, D. Schwab and W. Pfleging, *Laser-based Micro-and Nanoprocessing XVII*, 2023, pp. 83–91.

37 J. B. Habedank, D. Schwab, B. Kiesbauer and M. F. Zaeh, *J. Laser Appl.*, 2020, **32**, 1–6.

38 B. Jaeggi, B. Neuenschwander, M. Zimmermann, L. Penning, R. DeLoor, K. Weingarten and A. Oehler, *Laser Applications in Microelectronic and Optoelectronic Manufacturing (LAMOM) XIX*, 2014, pp. 150–159.

39 U. Loeschner, J. Schille, A. Streek, T. Knebel, L. Hartwig, R. Hillmann and C. Endisch, *J. Laser Appl.*, 2015, **27**, 1–7.

40 J. Schille, L. Schneider, A. Streek, S. Kloetzer and U. Loeschner, *Opt. Eng.*, 2016, **55**, 096109–096109.

41 J. Schille and U. Loeschner, *Ultrashort pulse lasers in high-rate laser micro processing–Quo vadis?*, 2021.

42 V. Scheck, R.-G. Scurtu, A. Innocenti, G. Carbonari, A. Hoffmann, M. Hölzle, P. Axmann and M. Wohlfahrt-Mehrens, *J. Power Sources*, 2024, **624**, 235528.

43 J. Kriegler, L. Hille, S. Stock, L. Kraft, J. Hagemeister, J. B. Habedank, A. Jossen and M. F. Zaeh, *Appl. Energy*, 2021, **303**, 117693.

44 M. Yamada, N. Soma, M. Tsuta, S. Nakamura, N. Ando and F. Matsumoto, *Int. J. Extreme Manuf.*, 2023, **5**, 035004.

45 L. Hille, M. P. Noecker, B. Ko, J. Kriegler, J. Keilhofer, S. Stock and M. F. Zaeh, *J. Power Sources*, 2023, **556**, 232478.

46 M. Keppeler, H.-Y. Tran and W. Braunwarth, *Energy Technol.*, 2021, **9**, 2100132.

47 M. Schmitt, M. Baunach, L. Wengeler, K. Peters, P. Junges, P. Scharfer and W. Schabel, *Chem. Eng. Process.*, 2013, **68**, 32–37.

48 P. S. Grant, D. Greenwood, K. Pardikar, R. Smith, T. Entwistle, L. A. Middlemiss, G. Murray, S. A. Cussen, M. J. Lain, M. Capener, *et al.*, *J. Phys.: Energy*, 2022, **4**, 042006.

49 Y. Liu, R. Zhang, J. Wang and Y. Wang, *iScience*, 2021, **24**, 1–17.

50 L. Torrisi, A. Borrielli and D. Margarone, *Nucl. Instrum. Methods Phys. Res., Sect. B*, 2007, **255**, 373–379.

51 N. Hodgson, A. Steinkopff, S. Heming, H. Allegre, H. Haloui, T. S. Lee, M. Laha and J. VanNunen, *Laser Applications in Microelectronic and Optoelectronic Manufacturing (LAMOM) XXVI*, 2021, pp. 21–41.

52 C.-H. Hung, S. Allu and C. L. Cobb, *J. Electrochem. Soc.*, 2025, 172–185.

53 C. L. Cobb and S. E. Solberg, *J. Electrochem. Soc.*, 2017, **164**, A1339.

54 M. D. Murbach, B. Gerwe, N. Dawson-Elli and L.-K. Tsui, *J. Open Source Softw.*, 2020, **5**, 2349.

55 J. Landesfeind, J. Hattendorff, A. Ehrl, W. A. Wall and H. A. Gasteiger, *J. Electrochem. Soc.*, 2016, **163**, A1373.

56 K. W. Knehr, J. J. Kubal, P. A. Nelson and S. Ahmed, *Battery performance and cost modeling for electric-drive vehicles (a manual for BatPaC v5.0)*, Argonne National Lab.(ANL), Argonne, IL (United States), technical report, 2022.

57 E. Ayl and E. Kocak, *Can. J. Chem. Eng.*, 2024, 1–39.

58 A. Cavalleri, K. Sokolowski-Tinten, J. Bialkowski, M. Schreiner and D. von der Linde, *J. Appl. Phys.*, 1999, **85**, 3301–3309.

59 J. König, S. Nolte and A. Tünnermann, *Opt. Express*, 2005, **13**, 10597–10607.

60 G. Raciukaitis, M. Brikas, P. Gecys and M. Gedvilas, *High-Power Laser Ablation VII*, 2008, pp. 725–735.

61 G. Raciukaitis, M. Brikas, P. Gecys, B. Voisiat, M. Gedvilas, *et al.*, *J. Laser Micro/Nanoeng.*, 2009, **4**, 186–191.

62 D. Wortmann, T. Mans and J. Weitenberg, International Congress on Applications of Lasers & Electro-Optics, 2009, pp. 856–860.

63 A. Slocombe and L. Li, *Appl. Surf. Sci.*, 2000, **154**, 617–621.

64 B. Bornschlegel and J. Finger, *J. Laser Micro/Nanoeng.*, 2019, **14**, 88–94.

65 E. Ohmura, I. Fukumoto and I. Miyamoto, Third International Symposium on Laser Precision Microfabrication, 2003, pp. 462–466.

66 M. Weikert, C. Foehl and F. Dausinger, Third International Symposium on Laser Precision Microfabrication, 2003, pp. 501–505.

67 A. Ancona, S. Döring, C. Jauregui, F. Röser, J. Limpert, S. Nolte and A. Tünnermann, *Opt. Lett.*, 2009, **34**, 3304–3306.

68 S. M. Eaton, H. Zhang, P. R. Herman, F. Yoshino, L. Shah, J. Bovatsek and A. Y. Arai, *Opt. Express*, 2005, **13**, 4708–4716.

69 J. Lopez, R. Torres, Y. Zaouter, P. Georges, M. Hanna, E. Mottay and R. Kling, *Frontiers in Ultrafast Optics: Biomedical, Scientific, and Industrial Applications XIII*, 2013, pp. 131–144.

70 J. Lopez, G. Mincuzzi, R. Devillard, Y. Zaouter, C. Hönninger, E. Mottay and R. Kling, *J. Laser Appl.*, 2015, **27**, 28008–28016.

71 L. Cangueiro, J. A. Ramos-de Campos and D. Bruneel, *Molecules*, 2021, **26**, 6327–6340.

72 J. Schille, L. Schneider and U. Loeschner, *Appl. Phys. A*, 2015, **120**, 847–855.

73 K. Du, S. Brüning and A. Gillner, *Laser-Based Micro-and Nanopackaging and Assembly VI*, 2012, pp. 174–183.

74 Y. Li, *Elements of Optical and Laser Beam Scanning: Modeling of Mirror and Prism Scanning Devices*, SPIE Press, 2021.

75 G. F. Marshall and G. E. Stutz, *Handbook of optical and laser scanning*, Taylor & Francis, 2012.

76 G. Römer and P. Bechtold, *Phys. Proc.*, 2014, **56**, 29–39.

77 I. Pangolin, Laser Systems, https://scannermax.com/pages/resonant-scanners.

78 S. L. Chen and E. S. Yeung, *Rev. Sci. Instrum.*, 1988, **59**, 2393–2396.

79 J. Khoury, B. Haji-Saeed, C. P. Morath, C. L. Woods, S. K. Sengupta and J. Kierstead, *Appl. Opt.*, 2006, **45**, 8177–8185.

80 J. Khoury, C. L. Woods, D. Pyburn, B. Haji-Saeed, S. K. Sengupta, D. B. Megherbi and J. Kierstead, Sinusoidal to Linear Scanning Correction using A Diffraction Grating, in *Frontiers in Optics 2004/Laser Science XXII/Diffractive Optics and Micro-Optics/Optical Fabrication and Testing*, OSA Technical Digest Series, Optica Publishing Group, 2004.

81 P. Bechtold, R. Hohenstein and M. Schmidt, *Opt. Lett.*, 2013, **38**, 2934–2937.

82 M. Gottlieb, C. L. Ireland and J. M. Ley, *Electro-optic and acousto-optic scanning and deflection*, Marcel Dekker, Inc, 1983.

83 H. Matsumoto, M. Unrath, J. Kleinert and H. Zhang, Applications and Technology, CLEO, 2014.

84 S. Bruening, G. Hennig, S. Eifel and A. Gillner, *Phys. Procedia*, 2011, **12**, 105–115.